Satellite-based Quantification of NOx Emissions from Global Oil and Gas Fields

Piyushkumar Patel[1], Ritesh Gautam[2,3], and Mark Omara[2,3]

[1]Affiliation not available
[2]MethaneSAT LLC
[3]Environmental Defense Fund

December 26, 2024

Abstract

Identifying air pollutant sources and quantifying related emissions provides crucial information towards improving global air quality and public health. Emission inventories commonly used for oil and gas (OG) activities inadequately represent nitrogen oxide (NOx) emissions, with notable discrepancies identified in the past. Satellite remote sensing provides a unique vantage point to map and quantify several key multi-pollutant species on a routine basis across the global scale. Here, we quantify annual NOx emissions from 44 major OG basins distributed globally, utilizing TROPOspheric Monitoring Instrument (TROPOMI) nitrogen dioxide (NO2) observations with the divergence flux method. In addition, we use the spaceborne Visible Infrared Imaging Radiometer Suite (VIIRS) natural gas flaring detections to further constrain satellite-derived NOx emissions. The divergence flux method, which addresses 3D topography corrections and chemical loss of NOx while accounting for wind-induced flux smearing, provides a robust approach for estimating NOx emissions. Our findings reveal a substantial level of NOx emissions from individual OG facilities and major production clusters as well as flaring activity, which serve as valuable data for assessing emission inventories. Subsequently, we conducted a comparative analysis between our TROPOMI-derived NOx emissions and those obtained from the existing EDGARv6.1 and CAMS-GLOB-ANT_v5.3 global emission inventories. This evaluation underscored a noteworthy disparity, with existing inventories significantly reporting lower emissions from the OG sector relative to TROPOMIderived data. Specifically, EDGAR exhibited a substantially lower estimate of onshore emissions by 61%, and CAMS displayed an even pronounced lower estimate by 78%, compared to TROPOMI-derived data from this study. For offshore emissions, EDGAR showed a similar pattern, albeit to a lesser extent, with a 26% underestimation, while CAMS showed a considerable underestimation of 92%. These findings hold significance for enhancing global NO2 emission inventories, particularly from OG fields, and therefore address gaps in current bottom-up inventories. Additionally, our approach yields detailed spatial emission maps, enhancing granularity in depicting NOx distribution. We further explore the variations in the correlation between NOx emissions with OG production volumes and CH4 concentrations across the different OG basins in North America, shedding light on their emissions characteristics and providing insights into the observed co-locations of methane and NOx emissions from oil and gas activity.

Satellite-based Quantification of NO_x Emissions from Global Oil and Gas Fields

Piyushkumar N. Patel[1], Ritesh Gautam[1,2], Mark Omara[1,2]

[1]*MethaneSAT LLC, Austin, TX, USA*
[1,2] *Environmental Defense Fund, Washington DC, USA*

Corresponding author email - piyushether@gmail.com and rgautam@edf.org

Abstract

Identifying air pollutant sources and quantifying related emissions provides crucial information towards improving global air quality and public health. Emission inventories commonly used for oil and gas (OG) activities inadequately represent nitrogen oxide (NO_x) emissions, with notable discrepancies identified in the past. Satellite remote sensing provides a unique vantage point to map and quantify several key multi-pollutant species on a routine basis across the global scale. Here, we quantify annual NO_x emissions from 44 major OG basins distributed globally, utilizing TROPOspheric Monitoring Instrument (TROPOMI) nitrogen dioxide (NO_2) observations with the divergence flux method. In addition, we use the spaceborne Visible Infrared Imaging Radiometer Suite (VIIRS) natural gas flaring detections to further constrain satellite-derived NOx emissions. The divergence flux method, which addresses 3D topography corrections and chemical loss of NO_x while accounting for wind-induced flux smearing, provides a robust approach for estimating NO_x emissions. Our findings reveal a substantial level of NO_x emissions from individual OG facilities and major production clusters as well as flaring activity, which serve as valuable data for assessing emission inventories. Subsequently, we conducted a comparative analysis between our TROPOMI-derived NO_x emissions and those obtained from the existing EDGARv6.1 and CAMS-GLOB-ANT_v5.3 global emission inventories. This evaluation underscored a noteworthy disparity, with existing inventories significantly reporting lower emissions from the OG sector relative to TROPOMI-derived data. Specifically, EDGAR exhibited a substantially lower estimate of onshore emissions by 61%, and CAMS displayed an even pronounced lower estimate by 78%, compared to TROPOMI-derived data from this study. For offshore emissions, EDGAR showed a similar pattern, albeit to a lesser extent, with a 26% underestimation, while CAMS showed a considerable underestimation of 92%. These findings hold significance for enhancing global NO_2 emission inventories, particularly from OG fields, and therefore address gaps in current bottom-up inventories. Additionally, our approach yields detailed spatial emission maps, enhancing

granularity in depicting NO_x distribution. We further explore the variations in the correlation between NO_x emissions with OG production volumes and CH_4 concentrations across the different OG basins in North America, shedding light on their emissions characteristics and providing insights into the observed co-locations of methane and NO_x emissions from oil and gas activity.

1 Introduction

Emissions of air pollutants including nitrogen oxides (NO_x), from various oil and gas (OG) sources, such as venting, flaring, combustion machinery, and leakage, have raised growing environmental concerns (Banerjee & Toledano, 2016; Duncan et al. 2016; Elvidge et al., 2018). Emissions of NO_x, comprising nitrogen monoxide (NO) and nitrogen dioxide (NO_2), are of utmost concern due to their central role in atmospheric chemistry, air quality, and climate. They serve as precursors to ground-level ozone (O_3), a key air pollutant with severe health implications, and contribute to the production of secondary aerosols and tropospheric ozone. Increased levels of tropospheric ozone, which result from NO_x and volatile organic compound (VOC) emissions, can have effects on respiratory and cardiovascular health issues (WHO, 2019). Additionally, elevated NO_2 levels pose direct health risks (Jacob, 1999). Given that anthropogenic activities linked to oil and gas extraction, refining, and combustion stand as an important source of NO_x emissions, there is a strong need for comprehensive assessment and monitoring. To mitigate these emissions and their adverse effects on the environment and public health, policy interventions and regulatory measures have been enacted within the fossil fuel energy sector (Falkner, 2016; Keohane & Oppenheimer, 2016). These efforts are crucial not only for mitigating climate change but also for promoting data transparency, a fundamental requirement under the Paris Agreement framework (Falkner, 2016)

The need to accurately track and quantify changes in air pollution and greenhouse gas emissions from OG operations has led to the development of independent observational methods (Alvarez, 2018; de Gouw et al., 2020; Dix et al., 2020, 2022; Edwards et al., 2014; Fedkin et al., 2024; Francoeur et al., 2021; Lauvaux et al., 2022; Omara et al., 2022, 2023; Shen et al., 2022; Zhang et al., 2019; Varon et al., 2024). Existing bottom-up emission inventories are often based on reported activities and dated emission factors and can lag behind regular monitoring observations. Therefore, satellite measurements, like those from TROPOspheric Monitoring Instrument (TROPOMI), can serve as important tool for providing regular and up-to-date information about emissions. Satellite-based approaches may offer valuable insights into the effectiveness of OG regulation and policy implementation. Notably, satellite-based observations have emerged as a reliable means of monitoring anthropogenic emissions, including those stemming from OG activities (Duncan et al., 2016; Fioletov et al., 2013; Li et al., 2016; Majid et al., 2017; McLinden et al., 2012, 2016; Zhu et al., 2014; Zhang et al. 2018). Such observations complement ground-based monitoring efforts (Alvarez, 2018; Gilman et al., 2013; Simpson et al., 2010; Zavala-Araiza et al., 2015). Satellite observations offer a unique advantage in providing complementary information about

emission sources, allowing for a more comprehensive understanding of underlying emission activity. For instance, spaceborne observations using the Ozone Monitoring Instrument (OMI) identified numerous large SO_2 sources, including offshore OG production clusters in the southern Gulf of Mexico and the Persian Gulf, which were absent from bottom-up emission inventories (McLinden et al., 2016; Zhang et al., 2019). Similarly, satellite-based studies have revealed increasing trends in NO_2 column densities in several North American OG production areas, such as Bakken, Eagle Ford, Permian, Niobrara-Codell in the United States, and Athabasca in Canada, largely attributed to expanding production between 2005 and 2020 (Dix et al., 2020, 2022; Laughner & Cohen, 2019; Li et al., 2016; Majid et al., 2017; Zhang et al., 2019)]

Satellite-based measurements utilize spectrally resolved observations, such as those acquired by the TROPOspheric Monitoring Instrument (TROPOMI) aboard the Sentinel-5 Precursor satellite. With its relatively high spatial resolution of 3.5 km x 3.5 km and daily global coverage, TROPOMI enables the identification of NO_x point sources with unprecedented accuracy (ATBD, https://sentinels.copernicus.eu/documents/247904/2476257/Sentinel-5P-TROPOMI-ATBD-NO2-data-products, last access: 7 April 2023), (Van Geffen et al., 2022). Consequently, TROPOMI has facilitated a series of studies examining the variability of NO_x in various regions, leading to the identification of specific emission sources and their emissions. The data from TROPOMI, and its predecessors, have offered valuable insights into NO_x point source emissions, allowing for more precise control of emission inventories and enhancements to existing data (Beirle et al., 2019, 2021, 2023). The application of a method based on the divergence of NO_2 column fluxes has been pivotal in quantifying NO_x emissions from point sources, along with the development of a fuel-based inventory for oil and gas operations by Francoeur et al., (2021), showcasing the potential of spaceborne data for emission estimation (Beirle et al., 2019; Goldberg et al., 2019; Lorente et al., 2019). These top-down approaches, which do not rely on complex atmospheric chemistry models, have proven to be computationally efficient and independent, providing annually updated emission estimates.

This study aims to estimate NO_x emissions originating from global oil and gas operations by leveraging TROPOMI retrievals. Our distinctive approach involves integrating natural flaring detection data from Visible Infrared Imaging Radiometer Suite (VIIRS) with TROPOMI-derived tropospheric NO_2 to identify global oil and gas (OG) operations on a global scale. Building upon previous research, our approach utilizes the flux-divergence method, used for the detection and quantification of NO_x emissions from point sources like power plants, as well as to calculate area emissions attributed to oil and gas fields. By harnessing the high spatial resolution and frequent coverage of TROPOMI data, we aim to provide detailed and up-to-date information on NO_x emissions from this sector. Moreover, we compare the TROPOMI-derived NO_x emissions with those from inventories such as EDGARv6.1 and CAMS-GLOB-ANT_v5.3 to assess emissions through the bottom-up approach. We also addressed the uncertainties associated with TROPOMI-derived NO_x emissions. The outcomes of our study will serve as a valuable resource for air quality management and policy-making, helping targeted reduction strategies and enabling effective monitoring of progress toward emission reduction goals.

2 Datasets

2.1 *TROPOMI NO_2*

The TROPOspheric Monitoring Instrument (TROPOMI), launched as part of the European Space Agency's Copernicus Sentinel 5 Precursor (S5P) satellite mission on October 13, 2017, is a pioneering Earth observation instrument. It orbits at an altitude of 825 kilometers in a sun-synchronous, low-Earth orbit, crossing the Equator at 13:30 local solar time. TROPOMI quantifies total column densities of trace gases across ultraviolet-visible-near-infrared (UV-VIS-NIR) and shortwave infrared (SWIR) spectral regions. TROPOMI offers exceptional spatial precision, with pixel sizes initially at 3.5 x 7 km^2, later refined to 3.5 x 5.5 km^2, covering a swath width of 2600 kilometers (Van Geffen et al., 2020, 2022). Its operational efficiency enables rapid Earth surface scans, providing global coverage in about 100 minutes daily.

NO_2 slant column densities from radiance measurements acquired within the 405–465 nm spectral range of the UV-VIS-NIR spectrometer. Tropospheric vertical column density data, representing the integrated number of NO_2 molecules per unit area from the surface to the tropopause, is derived by subtracting the stratospheric component and converting the tropospheric slant column into a vertical column employing an air mass factor (AMF). The AMF, a dimensionless quantity, depends on various parameters, including satellite viewing angles, solar angles, the effective cloud radiance fraction, atmospheric pressure, and the vertical distribution of NO_2 as simulated using the TM5-MP chemical transport model at a 1 x 1º resolution (Williams et al., 2017), and surface reflectivity (climatological Lambertian-equivalent reflectivity data at a 0.5 x 0.5º resolution; (Kleipool et al., 2008). It is noteworthy that operational AMF computation does not explicitly incorporate aerosol absorption effects, as these are addressed within the effective cloud radiance component.

For our analysis, we use the level 2 NO_2 tropospheric VCD (TVCD) from the v2.3.1 Product Algorithm Laboratory (PAL) product, which was released in December 2021 (Data was sourced from the S5P Pre-operations Data Hub, accessible at https://s5phub.copernicus.eu/dhus/). In contrast to earlier versions, this PAL product incorporates an enhanced FRESCO algorithm, which yielded notable improvements: higher cloud altitudes, reduced air mass factors (AMFs), and elevated tropospheric NO_2 columns. Furthermore, a refinement has been introduced involving a surface albedo correction based on observed reflectance, tailored explicitly for cloud-free scenes. This alteration has resulted in a general upswing in tropospheric NO_2 columns, particularly pronounced over regions characterized by higher pollution levels. According to findings reported by (Van Geffen et al., 2021), the net effect of this transition from v1.3 to v2.3.1 manifests as a roughly 13% increase in tropospheric vertical column NO_2 for cloud-free scenes, exhibiting spatial variability and accentuated elevations in areas with heightened pollution levels. To ensure data quality, TROPOMI NO_2 VCDs undergo filtering with a quality assurance threshold (> 0.75) and a solar zenith angle ($SZA \leq 65°$) to mitigate potential errors arising from the stratospheric correction and low-light conditions. Furthermore, to ensure optimal viewing conditions, selecting TROPOMI

pixels restricts the viewing zenith angles (VZA), limiting them to values below 56°. This criterion helps avoid less favorable viewing conditions, particularly at the edges of the satellite's swath. As a result, this restriction effectively limits the maximum pixel width across the track to 11 km. Subsequently, the filtered data are gridded onto a regular latitude/longitude grid with a spatial resolution of 0.01° × 0.01° using an optimal algorithm.

2.2 VIIRS Natural Gas Flaring Detections

We use natural gas flaring detection data from the Visible Infrared Imaging Radiometer Suite (VIIRS) instrument onboard the Suomi-National Polar-orbiting Partnership (S-NPP) satellite, a joint endeavor between NASA and NOAA, launched in October 2011 as a proxy to identify NO_2 plumes from OG sites. VIIRS offers observations twice daily near the equator, with extended coverage at higher latitudes due to orbit overlaps. These observations occur at approximately 1:30 p.m. (ascending node) and 1:30 a.m. (descending node), ensuring regular and comprehensive monitoring. The significance of VIIRS extends beyond its observational frequency. Notably, the S-NPP afternoon overpass aligns closely with the Sentinel-5P satellite's orbit, allowing for synergistic observations that enhance the accuracy and scope of our research.

For the detection of gas flares, (Elvidge et al., 2013) developed an algorithm that takes advantage of VIIRS nighttime capabilities in recording data in near- to short-wave infrared channels, particularly the VIIRS 750 m short-wave infrared (1.61 μm) channel and Day-Night Band (DNB) data. By focusing on nighttime observations, the algorithm effectively eliminates the influence of sunlight and pinpoints the radiant emissions of gas flares. Specifically, the algorithm capitalizes on the SWIR channel at 1.61 μm, which captures the peak radiant emissions from gas flares. Additionally, the 4-μm channel, commonly used for satellite fire detection, can identify larger flares. To underscore the global relevance of VIIRS Natural Gas Flaring Detections, (Elvidge et al., 2015) conducted a comprehensive survey of natural gas flaring. This survey provides valuable information, including estimates of gas-flared volumes for 7,467 individual sites. Users interested in annual global estimates up to 2020 can access this data at https://eogdata.mines.edu/download_global_flare.html. We harness VIIRS nighttime natural gas flaring data for our analysis in conjunction with TROPOMI tropospheric NO_2 VCDs. This combined dataset empowers us to identify emissions from oil and gas facilities, as depicted in *Figure 1*. However, it's imperative to acknowledge that while VIIRS data offers invaluable insights, certain limitations and uncertainties may be associated with its accuracy.

2.3 Meteorological Data

In addition to the TROPOMI NO_2 VCD data, meridional and zonal wind components, pressure, and temperature are required to determine the NO_x emission and lifetimes. The wind and meteorological parameters are provided by the ERA-5 reanalysis dataset from the European Centre for Medium-Range Weather Forecasts (ECMWF) on an hourly basis with a spatial resolution of 0.25° x 0.25° latitude/longitude. To align the wind and meteorological data with TROPOMI

observations, we interpolated the ERA-5 data onto the NO_2 spatial grid. We also performed temporal interpolation to match the local TROPOMI overpass for each study region. (Beirle et al., 2011) examined the influence of wind data level height on estimated NO_x emissions and lifetimes. Findings indicated a slight impact, with emissions and lifetimes changing less than 2% (5%) on average when wind data was taken from 200 meters (1000 meters) instead of 500 meters, with individual sources showing variations below 15%. Therefore, we use the horizontal winds at 100 and 10 meters from the EAR5 reanalysis data. The 100-meter wind was used to characterize horizontal transport in the planetary boundary layer, while the 10-meter wind represented the near-surface wind. Furthermore, we spatiotemporally interpolated horizontal winds at 100 and 10 meters from the ERA5 reanalysis to match TROPOMI Level 2 observations. By leveraging the ERA5 reanalysis dataset, we obtained the necessary meteorological variables to analyze atmospheric dynamics and transport patterns accurately.

2.4 *Ozone Climatology*

Ozone mixing ratios, used for the scaling of NO_2 to NO_x, were obtained from the Earth System Chemistry integrated Modelling (ESCiMo) project (Jöckel et al., 2016), using a specified dynamics simulation RD1SD-base-01. RD1SD-base-01 simulation is similar to the RC1SD-base-10 simulation but with an updated ECHAM5/MESSy Atmospheric Chemistry (EMAC) version, nudged (by Newtonian relaxation) towards ECMWF ERA-5 reanalysis data (Hersbach et al., 2020), and with boundary conditions (primarily emission inventories) according to the Chemistry -Climate Model Initiative (CCMI)-2 protocol (P. Jöckel, personal communication). The data has been online (i.e. during the simulation) sampled along the Sentinel 5P orbit as described by (Jöckel et al., 2010) (in section 5.4, submodel SORBIT). To accurately assess the NO_x/NO_2 ratio near the surface, it was essential to consider O3 concentrations extracted from the lowest layer of the model. This selection played a critical role in capturing the sensitivity of divergence to additional NO_x emissions at the emission source.

2.5 *Emission Inventories*

The Emissions Database for Global Atmospheric Research (EDGARv6.1) and the CAMS global anthropogenic emissions (CAMS-GLOB-ANT_v5.3) are both global emission inventories that provide monthly gridded emissions at a resolution 0.1°×0.1° across various sectors. EDGARv6.1 utilizes the activity data acquired from the International Energy Agency (IEA) and the Food and Agriculture Organization (FAO), covering various factors, including population, energy production, fossil fuel extraction, industrial processes, and agricultural statistics. Emissions in EDGARv6.1 are computed based on corresponding emission factors alongside national and regional data regarding technology mix and end-of-pipe measurements. This database encompasses the years from 1970 to 2018. CAMS-GLOB-ANT_v5.3 is a product developed within the Copernicus Atmospheric Monitoring Service framework, as comprehensively detailed by (Granier et al., 2019). In constructing this emissions inventory, NO_x emissions primarily draw

from various sectors outlined in the EDGARv5.0 emissions dataset, encompassing data up to 2015, which are extrapolated to 2021 relies on sector-specific trends gleaned from the Community Emissions Data System (CEDS) inventory, as expounded by (Hoesly et al., 2018) through 2019. Notably, sector nomenclature and definitions may exhibit variances when transitioning between different inventories. Both EDGARv6.1 and CAMS-GLOB-ANT_v5.3 implement a comprehensive methodology for estimating emissions at the country level. This methodology encompasses considerations such as technology deployment and the influence of emission factors contingent on fuel types and combustion conditions, in addition to activity data and low-resolution emission factors, as elucidated by (Janssens-Maenhout et al., 2019).

3 Methodology

3.1 Identification of OG sites

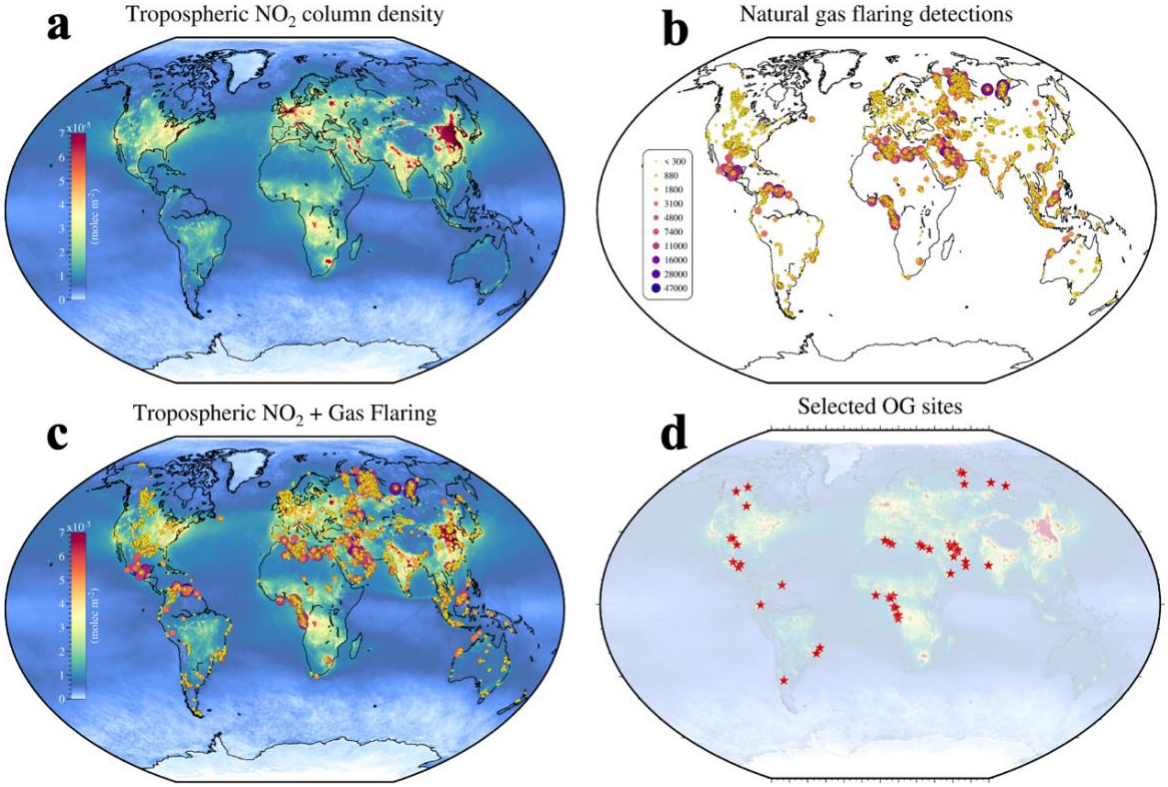

Figure 1 *(a) Global distribution of TROPOPMI-based tropospheric NO_2 VCD for the period January-December 2022, (b) global distribution of natural gas flaring detection from VIIRS observations, (c) collocated tropospheric NO_2 VCD and natural-gas flaring detections for identifying the oil and gas operations globally. (d) selected 44 OG sites, both offshore and onshore, for quantification of NO_x emission.*

The worldwide network of oil and gas infrastructure is extensive, intricate, and multifaceted. Identifying the NO_x emissions directly from TROPOMI datasets for OG sites poses challenges.

Consequently, we adopt VIIRS nighttime natural gas flaring data as a proxy for NO_2 plume detection, combined with TROPOMI tropospheric NO_2 VCDs, to discern NO_2 emissions originating from OG sites from January to December 2022. A two-step process is implemented to exclude NO_2 plumes resulting from transient occurrences like biomass burning or fire events. Initially, both TROPOMI and VIIRS data are subjected to annual averaging to pinpoint persistent NO_2 plume locations. Subsequently, these identified NO_2 plumes are cross-referenced with daily datasets to validate their persistence. Once the definitive NO_2 plumes associated with Oil and Gas (OG) sites are confirmed, their precise origin is visually verified using Google Maps to ensure that they emanate exclusively from OG sites. *Figure 1* illustrates the globally annual mean picture of TROPOMI tropospheric NO_2 VCDs (Figure 1a), VIIRS-based intensity of natural gas flaring detections (*Figure 1b*), collocated image of TROPOMI NO_2 VCD and VIIRS natural gas flaring detections (*Figure 1c*).

The natural gas flaring detections provide valuable spatial information on global upstream, midstream, and downstream natural gas flaring, revealing flaring hotspots in major oil and gas-producing countries, including those for which limited open-source data on oil and natural gas well locations are available (*Figure 1b, Figure 1c*). Detections were reported at over 10,000 facilities or groups of facilities worldwide (as seen in *Figure 1c*). This extensive dataset facilitates the identification of emission sources precisely and regional-scale emission characterization, as exemplified in recent studies by (Ialongo et al., 2021; Lyon et al., 2021; Shen et al., 2022; Zhang et al., 2020). These datasets are part of the Oil and Gas Infrastructure Mapping database (OGIM) V1 datasets (Omara et al., 2023). Nonetheless, it is worth noting that the VIIRS instrument operates at an approximate spatial resolution of about 750 m x 750 m at its nadir point (Elvidge et al., 2015). This presents challenges when attempting to associate VIIRS detections with specific oil and gas facilities, especially in regions like the Permian Basin in southern New Mexico and western Texas (USA), known for their high density of oil and gas infrastructure. Accurately attributing detections to individual facilities in spatially concentrated oil and gas regions demands additional investigation and research. The primary goal of this study is not to pinpoint the individual facilities or quantify NO_x emissions precisely. Instead, we aim to demonstrate the potential of modern satellite remote sensing technology in delineating the OG sites and mapping the extent of NO_x emissions across these areas. For this purpose, we have identified 44 specific OG sites (listed in *Table 1*), both onshore and offshore, illustrated in *Figure 1d*, for our subsequent analysis aimed at estimating NO_x emissions from space.

3.2 *Flux divergence method*

The typical outflow pattern of NO_2 TVCD, characterized by a signal decay with distance from the source point, reflects the interplay of atmospheric transport and nonlinear chemical processes. To address this, Beirle et al., (2019) proposed a flux divergence method aimed at estimating NO_x emissions and lifetimes by multiplying the mean NO_2 VCDs with the horizontal wind component. This method consists of applying the continuity equation in a steady state framework, where the combination of mass inflow into a specific pixel and emissions equals the

combination of mass outflow from the pixel and chemical loss. We employ a modified flux divergence method Beirle et al., (2019, 2021) to derive top-down NO_x emission maps. The central concept lies in the divergence of mass flux, which characterizes alterations in mass flow. A positive divergence value serves as an indication of a source. Consequently, we quantify NO_x emissions ($E$$NO_x$) by aggregating the contributions from both sources and sinks, as follows:

$$\boldsymbol{E_{NOx} = f_{NOx}\left(\nabla(V.u) + \frac{V}{\tau}\right)} \quad \textbf{(1)}$$

Here, the divergence term (D) were obtained by multiplying NO_2 VCDs (V) with the horizontal wind field (u) (along and across the swath tracks). The sink term is dominated by the chemical loss due to the reactions of NO_2 with OH, with a constant lifetime ($\boldsymbol{\tau}$). TROPOMI derived NO_2 VCD is scaled to NO_x by multiplying the scaling factor ($f$$NO_x$). Analyzing the flux divergence results in an emission estimate expressed in units of molec cm^{-2} s^{-1}. A step-by-step explanation of the emission estimation algorithm is provided in the subsequent sections.

3.2.1 Upscaling NO_2 to NO_x

In our study, we first converted the observed NO_2 columns for every TROPOMI pixel into the NO_x columns from which NO_x emissions are calculated directly instead of applying the fixed NO_x/NO_2 ratio of 1.32. To achieve this, we determine the scaling factor $f$$NO_x$ (in Eq. 1) by employing the principle underlying the photostationary steady state for polluted airmasses.

$$\frac{[\boldsymbol{NO_x}]}{[\boldsymbol{NO_2}]} = \mathbf{1} + \frac{[\boldsymbol{NO}]}{[\boldsymbol{NO_2}]} = \mathbf{1} + \frac{\boldsymbol{J}}{\boldsymbol{k}\,[\boldsymbol{O_3}]} \quad \textbf{(2)}$$

With the photolysis frequency of NO_2 (J) and the rate constant for the reaction of NO with O3 ($k[O3]$) (Seinfeld & Pandis, 2016). Ozone data are taken form a multi-year climatology model by ESCiMO (as described in section 2.4) simulation and converted into concentrations based on temperature and pressure from ERA5.

The photolysis frequency in the boundary layer for clear-sky conditions is parameterized as $J = 0.0167 \times \exp(-0.575 / SZA)$ s^{-1}, as proposed by (Dickerson et al., 1982), with solar zenith angle (SZA) taken from TROPOMI data product. The rate constant is parameterized as $k[O_3] = 2.07 \times 10^{-12} \times \exp(-1400/T)$ cm^{-3} $moelc^{-1}$ s^{-1}, as recommended by (Atkinson et al., 2004), with temperature T (in kelvin) from ERA5 reanalysis data. ERA5 reanalysis data were interpolated to TROPOMI overpass time and oversampled to the same spatial resolution.

3.2.2 Divergence

The divergence of the flux ($F = u.V$) in Eq. 1 is calculated as the derivative of horizontal wind (u) scaled NO_x column fluxes (V) (Beirle et al., 2019, 2021). The annual flux divergence, derived from

daily NO_x flux calculations, serves as an emission indicator in the planetary boundary layer (PBL), assuming a relatively constant free tropospheric NO_x fraction above the PBL, minimizing its impact on the divergence.

$$\boldsymbol{D = \nabla.\mathbf{F} = \nabla\,(uV) = u.\nabla V + V.\nabla u} \quad (3)$$

The first term ($u.\nabla V$) is represents advection (A) in meteorology, defined as the scalar product of horizontal wind vector and the spatial gradient of the TCVD. The second term ($V.\nabla u$) characterizes the divergence of wind fields scaled by the NO_x TVCD. However, our primary interest is on flux changes resulting from local NO_x emissions. Consequently, we calculate advection directly from Eq. 4 while explicitly excluding the influence of non-vanishing divergence of wind field. Nonetheless, the mean values of A and D exhibit remarkable similarity since the divergence of wind field is practically negligible over time.

$$\boldsymbol{A = u.\nabla V} \quad (4)$$

Beirle et al., (2021) identified systematic artifacts in divergence maps over mountainous regions, hindering NO_x quantification. In contrast, Sun (2022) introduced the "topography-wind" term (as seen in Eq. 5) to correct for these 3D transport effects, improving accuracy in emission estimates. The topography-wind term is calculated as:

$$\boldsymbol{C_{topo} = V/H_{sh}\ .w_0\ .\nabla Z_0} \quad (5)$$

with NO_x TVCD (V), H_{sh}, w_0, z_0 are the NO_x scale height, surface wind speed at 10 m and surface elevation, respectively. This correction term, known as the topography-wind term (C_{topo}) is calculated for each TROPOMI pixel using provided z_0 and w_0 at 10 m within the data product, assuming NO_x scale height of 1 km.

The topography-corrected advection (divergence as per Eq. 1) is then derived as:

$$\boldsymbol{A^* = A + f\ .C_{topo}} \quad (6)$$

The scaling factor (f) is empirically determined as 1.5, equivalent to a net NO_x scale height of 1/1.5 km = 667 m, to reducing the topography effects.

In Figure 2, we showcase a divergence map (computed using Eq. 6) for the Permian Basin, a largest OG production region in the United States. Positive values signify emission sources, while negative values are primarily associated with chemical loss, to be addressed in the sink term. Nevertheless, negative values could also result from factors like violation of steady state, statistical noise, or errors in the wind fields.

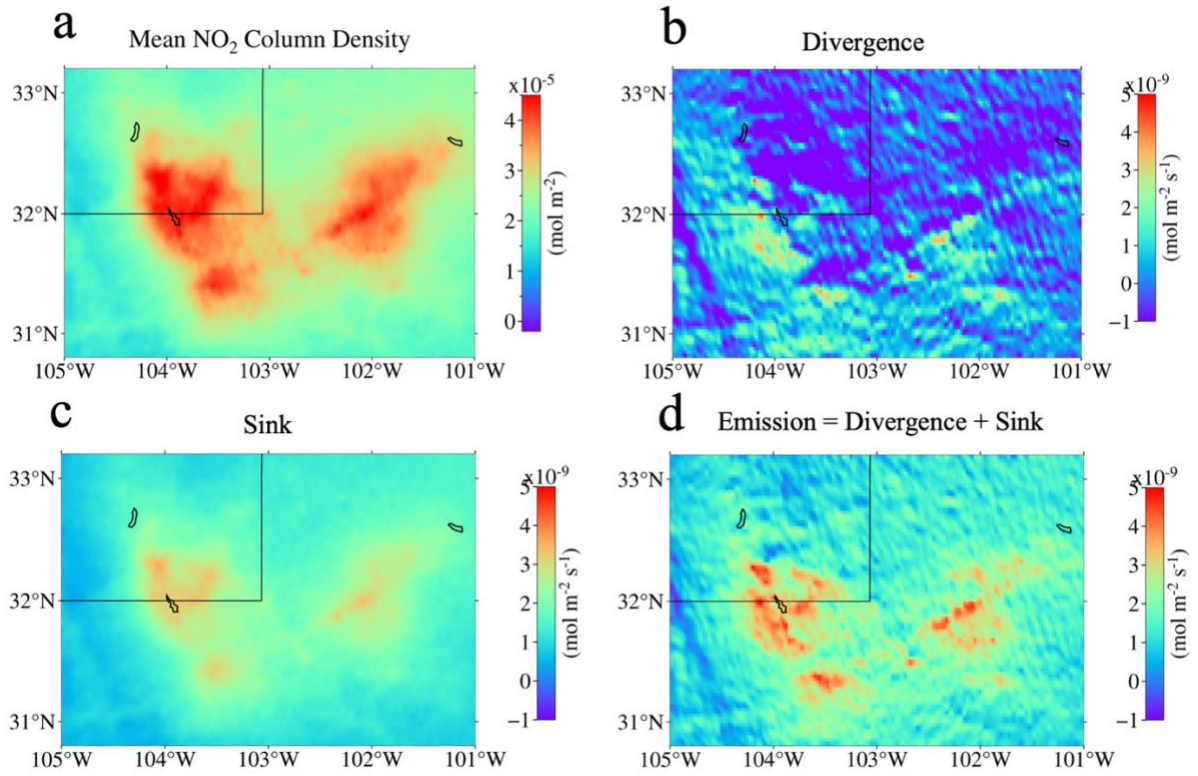

Figure 2: *Calculation of NO_x emission using TROPOMI NO_2 and the flux divergence method. (a) annual mean tropospheric NO_2 vertical column density, (b) calculated divergence, (c) calculated sink, (d) Calculated NO_x emissions (divergence and sink). The data shown here are an average over the full data set from January – December 2022.*

3.2.3 Sink

The sink process is primarily governed by the chemical loss of NO_x through the reaction with the hydroxyl radical (OH). Sinks of NO_x are included in the Eq. 1 by adding TVCD (V) divided by the atmospheric lifetime ($\boldsymbol{\tau}$) of NO_x. The effective lifetime ($\boldsymbol{\tau}$) can be approximated as the first-order loss to OH:

$$\boldsymbol{\tau = 1/\left(k_{OH+NO_2} \cdot [OH]\right)} \qquad \textbf{(7)}$$

The Master Chemical Mechanism (MCM; (Jenkin et al., 2003; Saunders et al., 2003) scheme is used to calculate the rate constant $k_{OH+}NO_2$ using pressure and temperature from ERA5. Despite the intricate nature of the instantaneous NO_x lifetime, constant NO_x lifetimes effectively link observed NO_2 TVCDs with NO_x emissions (Beirle et al., 2011; Goldberg et al., 2019; F. Liu et al., 2016). We determine OH concentrations using the method described by Dix et al., (2022), which relies on the empirical relationship between ozone photolysis frequency J($O(^1D)$) and OH concentrations, as established by Rohrer & Berresheim, (2006). The empirical correlation reveals a primarily linear relationship between J($O(^1D)$) and OH, consistently observed across various

seasons and locations, albeit with slight variations in slope and offset for the applied line fits. In our study, we utilize line fit parameters averaged from all documented campaigns:

$$OH = \ 3.38\,x\,10^{6}\,.\left(J\left(O^{1}(D)\right).10^{5}\right)^{0.956} + 0.162\,x\,10^{6} \qquad (8)$$

OH and J($O(^1D)$) are expressed in units of 10^6 cm^{-3} and 10^{-5} s^{-1}, respectively. The calculation of J($O(^1D)$) depends on solar zenith angle. We have excluded both the lifetime and background corrections, as performed in Beirle et al., (2019) and Dix et al., (2022), to eliminate free-tropospheric NO_x with a prolonged lifetime and different fNO_x. This exclusion has no impact on divergence calculation since additive terms are nullified.

4 Comparing Satellite-derived NOx emission with existing emission inventories

In our extensive global assessment, we analyzed NO_x emissions as derived from TROPOMI and conducted a rigorous comparative analysis against two prominent emission inventories, namely EDGARv6.1 for the year 2018 and CAMS-GLOB-ANT_v5.3 spanning 2019-2022. Notably, the year 2020 is omitted from the CAMS dataset due to a substantial reduction in NOx emissions attributable to the COVID-19 pandemic. Utilizing a 0.1°×0.1° sectorial gridding approach for both inventories, we aggregated emissions across various activity sectors to directly obtain estimates of anthropogenic NO_x emissions over the same geographic domain. Our examination encompassed a global scale, and Figure-3 offers a comprehensive visualization of the comparative emissions data from TROPOMI, EDGAR, and CAMS. The outcomes of our analysis revealed noteworthy discrepancies between the emission estimates originating from TROPOMI and those from the established EDGAR and CAMS inventories. Particularly, CAMS-GLOB-ANT reported lower average emissions, while EDGAR's NO_x emission estimates contrasted with TROPOMI's assessments. These disparities bring to the forefront the intricacies and variations inherent in the methods employed for quantifying emissions between TROPOMI and conventional inventory systems. The dissimilarities in reported emission levels underscore the diverse underlying assumptions, data sources, and methodologies applied in the estimation of NO_x emissions. Such variations in estimation approaches carry significant implications for the interpretation and utilization of emissions data, underscoring the imperative need for comprehensive and precise emission quantification to effectively inform policy decision-making. In our comprehensive analysis, we particularly emphasized the oil and gas sectors due to their pivotal role in emissions management. The variances observed in the sectoral allocation of emissions in these inventories further underline the necessity for enhanced accuracy and consistency in emission inventories, with particular attention to sectors as critical as oil and gas.

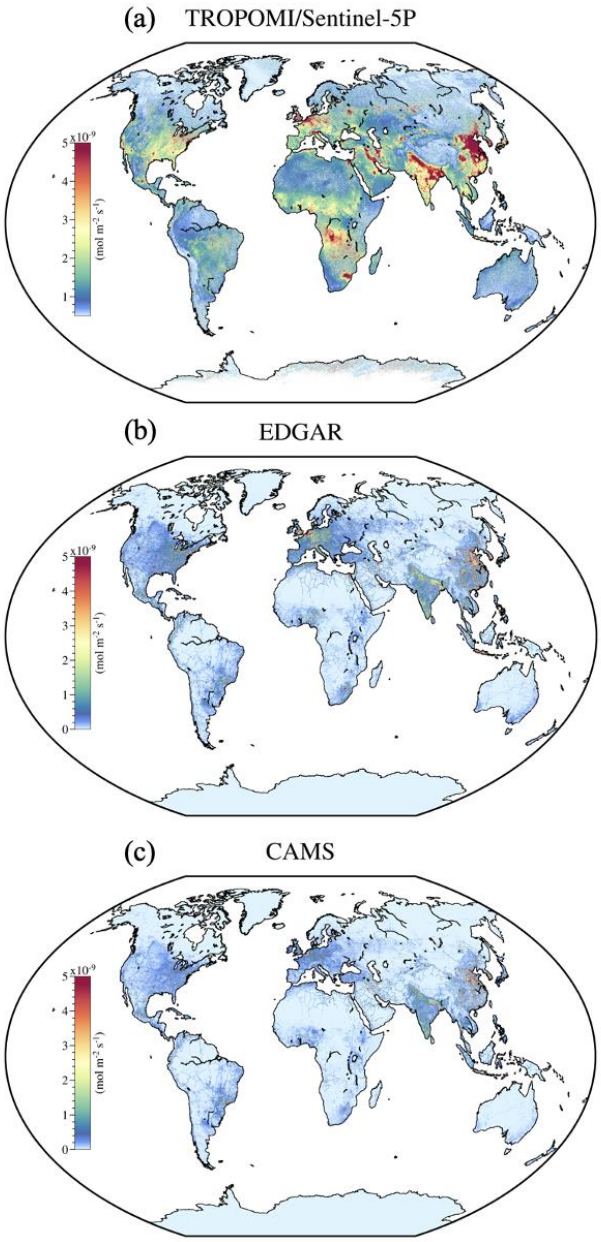

Figure 3: *(a) Calculated NO_x emission using TROPOMI observations using flux divergence method, (b) NO_x emission from EDGAR (EDGARv6.1) inventory, (c) NO_x emission from CAMS (CAMS-GLOB-ANT_v5.3) inventory.*

4.1 *Comparing regional NO_x emissions*

Utilizing the method described in section 3.2, we computed the annual average NO_x emissions for the year 2022 across 44 oil and gas production regions worldwide. The net NO_x emissions for each study area are quantified as the sum of emissions above zero within the region of interest. The borders of each study area were optimized to include significant signals over OG production areas and exclude other significant NO_x sources, but some contamination from other

sources might remain. The results are visually presented in Figure 4 & 5 and S1-S4 and their NO_x emissions from TROPOMI, EDGAR and CAMS and their relative differences are listed in Table 1. For instance, Figure-4 represents the tropospheric NO_2 vertical column density (VCD) following by corresponding NO_x emission from TROPOMI, EDGAR and CAMS in subsequent panels, focusing on three (a. Permian Basin, USA, b. Sureste onshore, Mexico, c. Sureste offshore, Mexico, d. Eagle Ford, USA and e. Bakken Basin, USA) oil and gas fields.

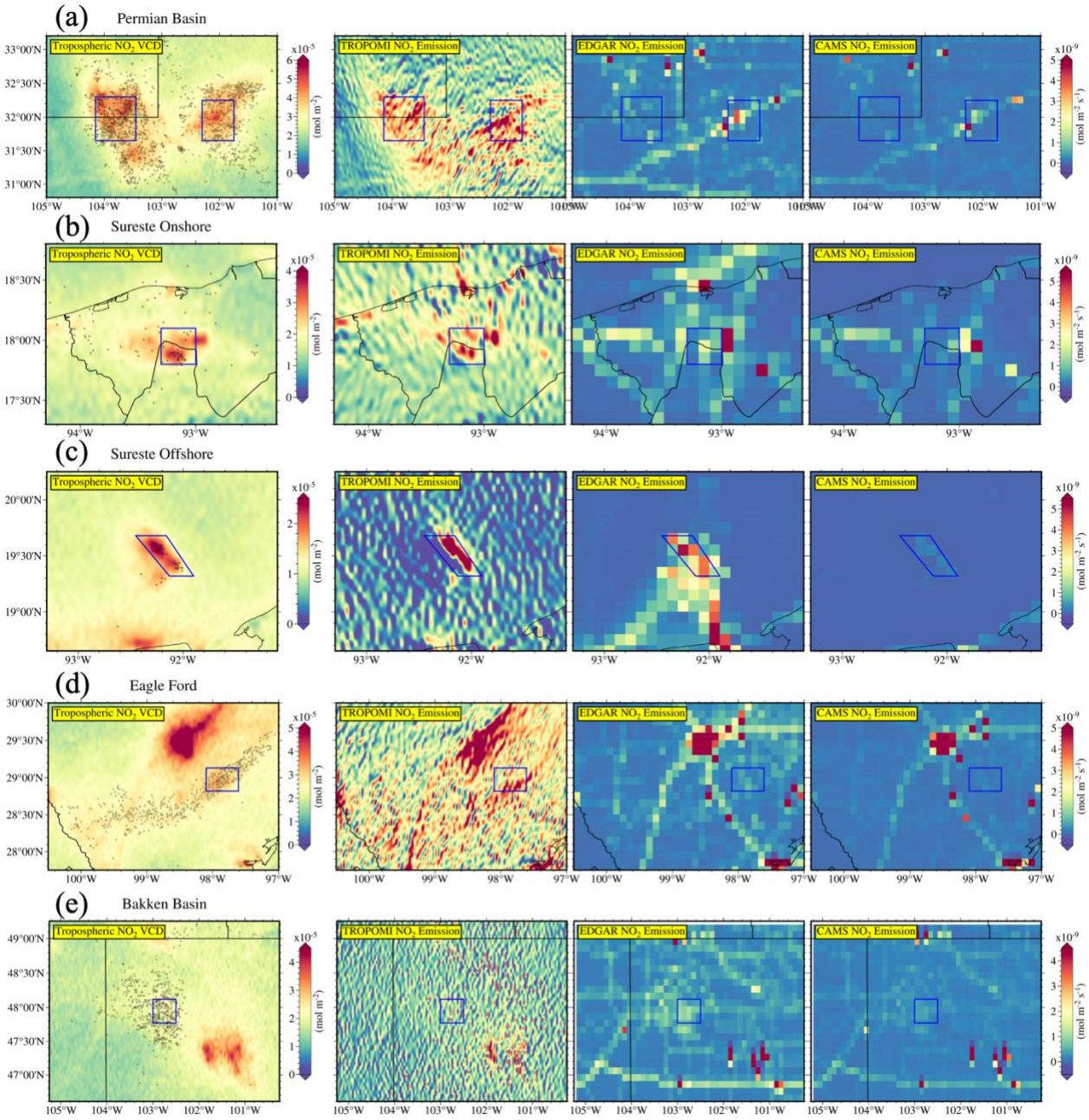

Figure 4: *Spatial distribution of tropospheric NO_2 vertical column density as derived from TROPOMI is presented in the initial panel, followed by the corresponding NO_x emissions from TROPOMI, EDGAR, and CAMS in subsequent panels. This analysis is centered on three (a.*

Permian Basin, USA, b. Sureste onshore, Mexico, c. Sureste offshore, Mexico, d. Eagle Ford, USA and e. Bakken Basin, USA) oil and gas fields.

Emissions from TROPOMI analysis ranged between 2,370 and 131,346 T yr^{-1} across the 33 onshore sites globally (seen in Table 1). The EDGAR NO_x emissions data generally underestimate the magnitude when compared to NO_x emissions derived from our TROPOMI analysis, with discrepancies ranging from 48% to 91% across the onshore OG regions examined. These discrepancies may be attributed to the inherent limitations of bottom-up inventories, which rely on reported data and may not fully account for the dynamic and complex nature of local OG activities. On the other hand, it appears that CAMS contains limited information to capture the NO_x emissions. . The CAMS data indicates its own set of underestimations, with deviations ranging from 65% to 96% assss compared to TROPOMI derived NO_x emissions. The Permian (Figure 4a) and Bakken (Figure 4e) basins, which are major oil producing basins in the US, exhibited notably high NO_x emissions (Permian is the largest oil producing basin in the US). The most substantial underestimations were observed in the Delaware sub-basin of the Permian basin (Figure 4a), where NO_x emissions reported by EDGAR and CAMS were approximately 91% and 95% lower, respectively, than those derived from TROPOMI. Similarly, other OG regions such as Al Ahas in Saudi Arabia (Figure 5b) and Safer in Yemen (Figure 5d), exhibited high NOx emissions and considerable discrepancies between TROPOMI-derived NOx emissions and those reported by EDGAR and CAMS. Varon et al., (2024) also detected and reported the elevated NOx emissions from power plants in the Al Ahas sites in Saudi Arabia. These noteworthy discrepancies may be reasonably ascribed to variations in local OG production activities, effectively captured by TROPOMI's high-resolution measurements but posing challenges for existing inventories with coarser spatial resolution to detect. In addition, the Athabasca OG basin in Canada (Figure S1) displayed underestimations of around 70% and 87% for EDGAR and CAMS, respectively. Our analysis considered a typical low bias of approximately 20% in TROPOMI-derived tropospheric NO_2 measurements in heavily polluted regions, potentially even greater when estimating near-surface NO_x emissions. Consequently, our calculated NO_x emissions should be regarded as conservative estimates, representing a lower limit.

Nevertheless, specific OG sites, including Bakken (Figure-4e), Misantla (Figure 5a) and Cocoa (Figure 5c) basins, which exhibited elevated NOx emissions, shows relatively minimal deviations between TROPOMI-derived NO_x emissions and those reported by EDGAR and CAMS. The Misantla basin in Mexico displayed relatively small deviations between TROPOMI NO_x emissions and those reported in EDGAR and CAMS, with an underestimation of approximately 6% and 9%, respectively. This can be attributed to the remote location of the Misantla basin, which experiences limited influence from urban or other emission sources. Likewise, the Bakken basin displayed relatively minor discrepancy in NO_x emissions between TROPOMI and EDGAR, amounting to around 25%, but a substantial variation of approximately 73% was found between TROPOMI and CAMS. Despite its considerable distance from urban areas in this study, there was a 25% underestimation of NO_x emissions in EDGAR. However, CAMS had difficulty to capture OG sources, perhaps because of the proximity of the basin to mountain ranges. In the case of the

Cocoa basin, there was an underestimation of approximately 18% and 45% in EDGAR and CAMS, respectively. This remarkable discrepancy can be attributed to the remote location of the Cocoa basin, which experiences limited influence from urban or other emission sources.

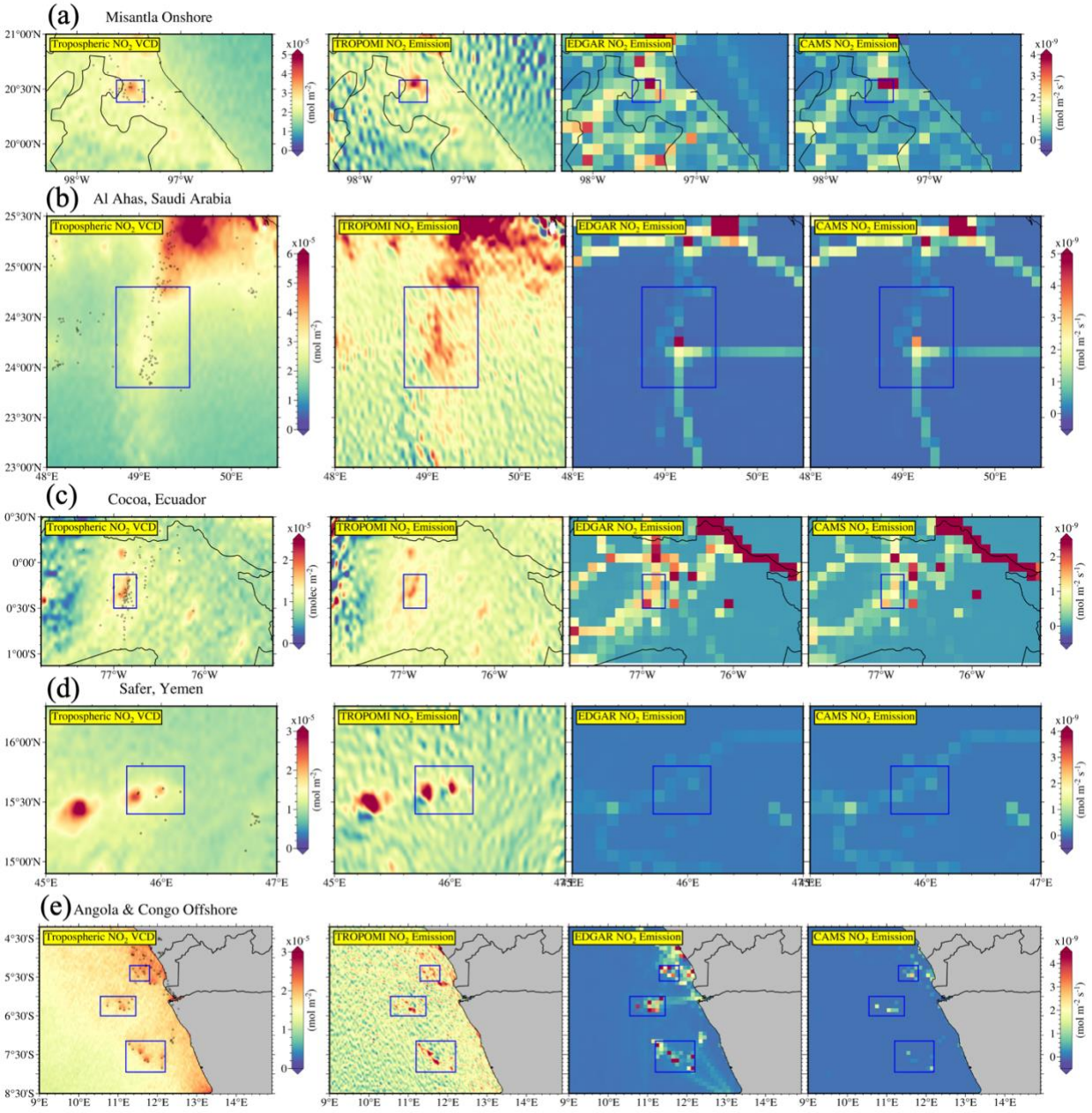

Figure-5: *Spatial distribution of tropospheric NO_2 vertical column density as derived from TROPOMI is presented in the initial panel, followed by the corresponding NO_x emissions from TROPOMI, EDGAR, and CAMS in subsequent panels. This analysis is centered on three (a. Misantla Onshore, Mexico, b. Al Ahas, Saudi Arabia, c. Cocoa, Ecuador, d. Safer, Yemen and e. Angola & Congo Offshore) oil and gas fields*

Our in-depth analysis underscores the variability in NO_x emissions across these OG sites and emphasizes the critical importance of employing high-resolution measurements, such as those

provided by TROPOMI. These high-resolution measurements can accurately assess and monitor these emissions, especially in regions where substantial discrepancies exist between bottom-up inventories like EDGAR and CAMS. Moreover, the observed differences between TROPOMI and EDGAR can be attributed to multiple factors. Cloud and solar zenith angle filtering in TROPOMI may lead to uneven data statistics in NO_2 VCDs, leaving some areas within a region under-sampled. Furthermore, drilling rigs in OG activities are not stationary sources of NO_x emissions, as the drilling process involves moving from one well site to another, which can result in uneven sampling of NO_2 VCDs and missing drilling-related emissions. On the other hand, discrepancies associated with the EDGAR inventory may arise because it assumes emissions to be consistent throughout a 24-hour daily cycle, which may not hold true in reality. Additionally, the distribution of state-level fuel volumes to individual wells in the EDGAR inventory can introduce uncertainties. Despite these potential sources of discrepancies, TROPOMI-derived emission maps offer valuable information on the spatial distribution of NO_x emissions resulting from oil and gas production activities, particularly in areas characterized by higher emission levels. These findings are important for enhancing our understanding of emissions, supporting effective air quality management, and informing policymaking by providing high-resolution observations of emissions from oil and gas activities.

In contrast to onshore sites, we broaden our investigation to encompass eleven offshore oil and gas (OG) production sites spanning across the globe (seen in Figure 4c, 4e and few more shown in supplementary figures S1 – S5). What emerges from this comprehensive examination is a strikingly diverse range of NO_x emissions, quantified by TROPOMI, with values spanning from 2,898 to 37,892 T yr-1 across these offshore OG regions. One of the most intriguing aspects of our findings lies in the substantial high estimates observed in the NO_x emissions calculated by TROPOMI when compared to those derived from the EDGAR and CAMS inventories. This consistent pattern most notably pronounced at offshore sites where the influence of urban areas is almost nonexistent, suggests that TROPOMI data are affective in reliably capturing the spatial distribution of NO_x emissions stemming from offshore OG activities. This result implies that TROPOMI's high-resolution measurements are particularly effective in regions where urban influence is minimal. The contrasting performance of the EDGAR inventory at offshore sites, compared to its performance at onshore sites, merits further exploration. At onshore sites, EDGAR tends to underestimate emissions by 14% to 57%. However, the data reveal that at offshore sites, EDGAR provides relatively better agreement with TROPOMI, implying less underestimation in comparison to onshore sites. Several factors contribute to this intriguing outcome: the isolation of offshore sites from urban areas, resulting in reduced urban influence; the more stable and consistent nature of offshore emissions due to more stationary offshore drilling platforms; and the distinct wind patterns that characterize offshore areas, facilitating the efficient dispersion of emissions. These factors collectively contribute to the improved agreement between TROPOMI and EDGAR in the context of offshore emissions. In contrast, a significant discrepancy arises in the performance of CAMS, which consistently struggles to capture the NO_x emissions from offshore OG sites. Consequently, CAMS NO_x emissions are found to be severely underestimated,

with underestimations exceeding 90% across all sites, and even surpassing 97% in 85% of offshore OG sites. This substantial underestimation underscores limitations of CAMS in representing NO_x emissions from offshore locations accurately.

In conclusion, our expanded analysis not only highlights the variability in NO_x emissions from offshore OG sites but also underscores the crucial role of high-resolution measurements, such as those provided by TROPOMI, in comprehensively assessing and monitoring emissions. Additionally, it emphasizes the significance of urban influence and wind patterns in influencing the discrepancies between TROPOMI, EDGAR, and CAMS measurements.

Table 1: Comprehensive summary of NO_x emissions derived from TROPOMI, EDGAR, and CAMS for 44 oil and gas (OG) sites worldwide. The last two columns detail the relative percentage differences in NO_x emissions between TROPOMI and EDGAR, as well as TROPOMI and CAMS, offering insights into the variations in emission estimates across these datasets.

OG Sites	**Country**	**Lat | Long**	**Area (in km^2)**	**TROPOMI NO_2 emission (T yr^{-1})**	**EDGAR NO_2 emission (T yr^{-1})**	**CAMS NO_2 emission (T yr^{-1})**	**Percentage Difference (TROPOMI - EDGAR) (%)**	**Percentage Difference (TROPOMI - CAMS) (%)**
Offshore	Angola	-7.55|11.70	10159.41	27207.9	11549.0	668.3	57.55	97.54
Offshore	Cameroon	4.27|8.38	1658.99	6061.8	6505.0	2667.5	-7.31	55.99
Offshore	Democratic Republic of the Congo	-6.25|11.00	5747.28	15956.3	8654.0	999.2	45.76	93.74
Elborma	Algeria	30.95|8.10	3006.48	7886.7	247.0	46.8	96.87	99.41
Offshore	Gabon	-1.35|8.75	1946.62	5309.8	1493.7	231.8	71.87	95.63
Divangui	Gabon	-1.92|9.90	1298.12	4327.6	482.6	200.7	88.85	95.36
Offshore	Ghana	4.55|-2.87	3483.51	8366.0	7206.6	191.1	13.86	97.72
Hassi Messaoud	Algeria	31.70|6.05	2291.55	9581.3	4926.3	2272.8	48.58	76.28
Hassi R'mel	Algeria	32.90|3.25	4569.87	12955.6	3522.6	2097.5	72.81	83.81
Offshore1	Nigeria	3.48|5.56	929.84	2898.8	2000.2	79.7	31.00	97.25
Offshore2	Nigeria	3.14|6.80	2389.13	6211.2	5031.9	23.5	18.99	99.62
Offshore	Republic of Congo	-5.40|11.55	2585.46	8583.3	6358.6	1055.8	25.92	87.70
Athabasca Basin	Canada	57.18|-111.63	9938.61	43270.5	12712.1	5488.9	70.62	87.31
Grande Prairie Basin	Canada	54.50|-118.60	3366.17	4721.5	1278.6	1024.8	72.92	78.30
Mumbai Offshore	India	19.40|71.33	2867.91	9910.8	6254.9	9.6	36.89	99.90
Misantla	Mexico	20.48|-97.49	810.03	3211.8	3009.5	2914.9	6.30	9.24
Sureste Offshore	Mexico	19.50|-92.18	2756.00	12042.6	13174.8	734.7	-9.40	93.90
Sureste Onshore	Mexico	17.95|-93.15	1284.35	5025.5	1702.2	737.3	66.13	85.33
Agiba-Meleiha	Egypt	30.75|27.05	4764.94	9591.3	4918.6	1729.0	48.72	81.97
Matrouh	Egypt	29.70|28.60	4415.75	9895.3	3047.8	962.8	69.20	90.27
Rasgarib	Egypt	28.20|33.25	15682.06	62917.4	45139.2	3821.9	28.26	93.93
Alahas	Saudi Arabia	24.30|49.15	11061.69	39264.3	4283.4	3264.7	89.09	91.69
Ar Rumaylah	Iraq	30.43|47.55	6700.75	131346.7	33234.7	29657.2	74.70	77.42
Gachsaran	Iran	30.20|50.65	6178.78	24453.9	7711.3	5734.6	68.47	76.55

Southpars	Iran	27.63|52.40	11110.92	138724.8	55185.3	68514.2	60.22	50.61
Mukhaizna	Oman	19.35|56.35	4727.47	9121.0	1096.5	290.8	87.98	96.81
Saihrawl	Oman	21.55|56.55	6677.41	14668.8	6771.1	3292.7	53.84	77.55
Safer	Yemen	15.60|45.95	2673.57	6033.0	196.6	237.5	96.74	96.06
Wafra-Burgan	Kuwait	28.80|47.90	5234.89	79905.2	23368.8	8940.6	70.75	88.81
Offshore	Persian Gulf	26.70|52.10	6817.10	21480.0	23326.3	2804.4	-8.60	86.94
Evenkiysky	Russia	60.40|96.35	3734.49	4121.1	135.5	4.1	96.71	99.90
Nadymsky	Russia	66.95|75.55	3546.75	3384.3	101.2	0.4	97.01	99.99
Khanty-Mansi	Russia	60.73|72.75	8263.37	12583.3	5957.5	1139.8	52.66	90.94
Yamalo-Nenets	Russia	66.25|77.05	14421.47	17088.3	20064.1	18765.4	-17.41	-9.81
Ust-Kutsky	Russia	58.10|106.70	5853.97	6810.7	2278.3	51.5	66.55	99.24
Cocoa	Ecuador	-0.32|-76.88	1216.16	2370.8	1943.4	1289.8	18.03	45.60
Maturin	Venezuela	9.66|-63.52	498.29	2851.5	1383.0	820.5	51.50	71.23
Neuquen	Argentina	-38.40|-68.68	3034.49	6325.8	6091.9	1195.7	3.70	81.10
Offshore	Rio de Janeiro	-22.35|-40.00	14935.29	24653.3	26391.8	518.3	-7.05	97.90
Offshore	São Paulo	-25.15|-42.70	20970.13	37892.6	18439.9	461.6	51.34	98.78
Eagle Ford	USA	28.98|-97.86	2299.88	10280.4	1416.1	746.1	86.23	92.74
Bakken Basin	USA	47.95|-102.75	3386.36	7849.4	5864.2	2108.9	25.29	73.13
Delaware, Permian Basin	USA	31.95|-103.75	5585.45	32363.7	2897.4	1543.0	91.05	95.23
Midland, Permian Basin	USA	32.00|-102.08	4169.19	22516.4	4864.4	8000.5	78.40	64.47

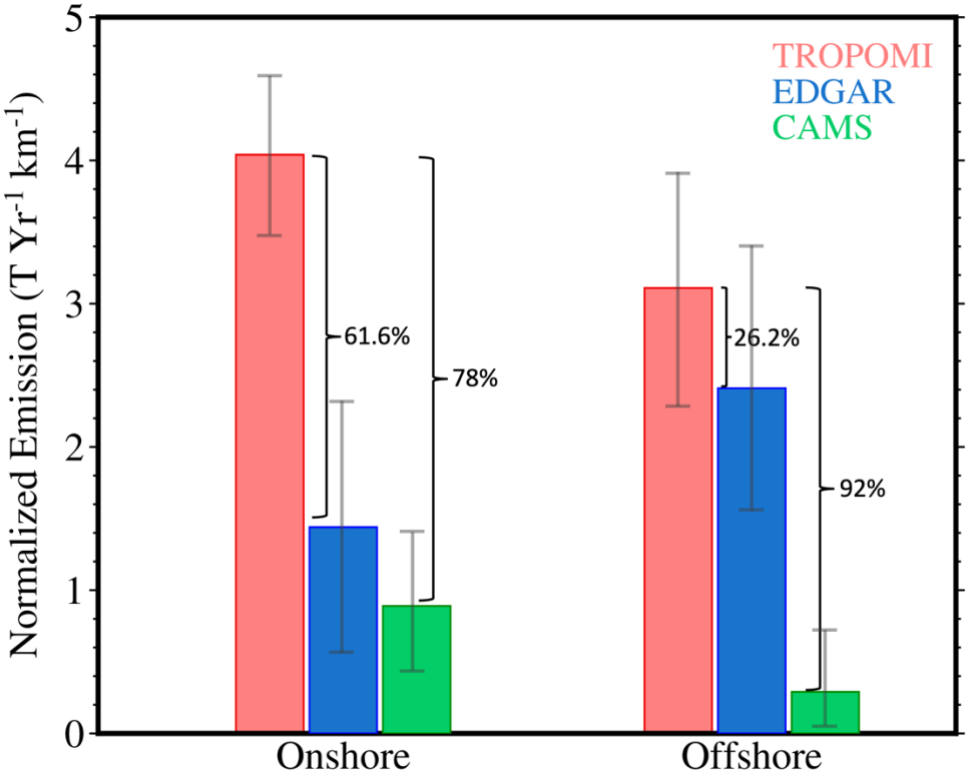

Figure 6: *Comparison of normalized NO_x emission from TROPOMI, EDGAR, and CAMS over the 44 onshore and offshore OG sites distributed globally (33 onshore and 11 offshore) . The normalized emissions are calculated firstly by dividing the individual site-wise NO_x emission by their total area in km and then averaged annually. Later, the sites are segregated into offshore and onshore sites and averaged the normalized emission values. Gray semi-transparent bars shows the standard deviation in the normalized emissions within the various OG sites included in the particular category.*

4.2 Global NOx comparisons

In our comprehensive assessment of NO_x emissions from 44 Oil and Gas sites across the globe, we systematically categorized these sites into onshore and offshore locations, with 33 and 11 sites, respectively. To facilitate meaningful comparisons, we calculated normalized emissions by dividing TROPOMI-derived NO_x emissions for each site by their corresponding areas. These normalized emissions were then averaged separately for onshore and offshore sites. Figure 6 illustrates the comparison of annually averaged normalized NO_x emissions from TROPOMI, EDGAR, and CAMS, grouped into onshore and offshore sites. Subsequently, we contrasted our findings with the NO_x emissions estimates provided by established bottom-up inventories, specifically EDGAR and CAMS. The results presented a significant contrast between onshore and offshore sites (as seen in Figure 6). For onshore sites, both EDGAR and CAMS exhibited significant underestimations, with EDGAR underestimating by 61% and CAMS by a stronger 78%

compared to TROPOMI-derived NO_x emissions. This substantial discrepancy between satellite-detected emissions and inventory-based estimates may be attributed to several factors. Onshore areas are more susceptible to the influence of background NO_x emissions, originating from urban centers and recurrent fire events. The urban environment contributes significantly to the pool of NO_x emissions, and these emissions can skew inventory-based estimates, leading to substantial underestimations. However, the situation differs for offshore sites. Emission estimates from EDGAR for offshore sites are notably closer to the actual TROPOMI-derived NO_x emissions, underestimating by 26%. This closer comparison can be attributed to the reduced influence of background emissions in offshore areas. These sites are more remote and less impacted by urban centers and associated emissions, thereby resulting in more accurate EDGAR-based estimates. In contrast, CAMS exhibits a much higher underestimation for offshore sites, at 92%, compared to TROPOMI-based emissions. This significant underestimation may be due to inherent limitations of CAMS in capturing emissions from such offshore areas accurately. In summary, the discernible discrepancies in underestimation between onshore and offshore sites underscore the intricate interplay between emissions from various sources and background contributions, necessitating the implementation of region-specific environmental management strategies.

4.3 *Uncertainties in TROPOMI-derived tropospheric NO_2 and NO_x emissions*

Quantification of NO_x emissions from global oil and gas fields using TROPOMI datasets with the flux divergence method is a complex endeavor that may be affected with uncertainties. These uncertainties stem from various sources, including the TROPOMI datasets, the NO_2 retrieval algorithm, assumptions made during algorithm development, limitation of the divergence flux method, and parameter estimation. To gain a comprehensive understanding of the uncertainties associated with this approach, we delve into these sources of uncertainty in detail:

4.3.1 Uncertainties in TROPOMI dataset

The precise estimation of tropospheric NO_2 column density data using TROPOMI is an invaluable resource for emissions quantification; however, it is accompanied by inherent uncertainties that warrant thorough consideration. These uncertainties originate from various facets of the retrieval process and significantly influence the robustness of the data. Firstly, the accuracy of slant column density (SCD) measurements is challenged by measurement noise and spectral fitting errors, which are well-documented sources of uncertainty in satellite-based observations (Boersma et al., 2004). Accurately distinguishing between stratospheric and tropospheric NO_2 is a crucial step in the retrieval process, and errors in this separation process can introduce significant uncertainties (Boersma et al., 2007). One of the most substantial contributors to the overall uncertainty is the calculation of tropospheric air mass factors (AMF), which are highly dependent on several parameters. These include surface albedo, a priori NO_2 profile, cloud fraction, and cloud pressure (Boersma et al., 2004; De Smedt et al., 2018). A crucial factor to consider is the impact of aerosols on the measurement. Errors in aerosol fraction assumptions, particularly near the Earth's surface compared to the true vertical profile, can lead to an

overestimation of tropospheric AMF, consequently resulting in an underestimation of tropospheric NO_2 vertical column density (VCD) (Boersma et al., 2004). It is also important to note that systematic underestimations of high NO_2 concentrations have been observed, particularly in highly polluted regions, due to spatial variability and inherent retrieval challenges (Shaiganfar et al., 2011). While temporal and spatial averaging can mitigate random errors, systematic errors are expected to persist if not adequately accounted for. As a whole, these uncertainties can range from 30% - 60% (Liu et al., 2021), underlining the critical necessity of acknowledging and quantifying these uncertainties to ensure the accurate interpretation of TROPOMI-derived data for emissions estimation and the consequential policy and decision-making processes. Continuous efforts to refine retrieval algorithms and enhance data quality aim to reduce these uncertainties over time.

The use of satellite data introduces a systematic clear-sky bias, as it relies on measurements from predominantly cloud-free days, limiting specific emission patterns from cloudier days. This limitation also impacts estimates of chemical lifetimes, resulting in systematic underestimations due to increased photolysis rates on cloudless days. Additionally, emissions and lifetimes are derived from early afternoon measurements, introducing a temporal bias. To delve deeper into temporal variability, future sensors on geostationary satellites could offer valuable insights.

Moreover, it is imperative to recognize that TROPOMI retrievals exhibit biases due to air mass factor estimation challenges and local effects, especially under varying vertical conditions. Recent versions of TROPOMI datasets (v2.x) indicate tropospheric vertical column densities 10-40% larger than earlier versions (v1.x), dependent on pollution levels and seasons (Van Geffen et al., 2021). The use of the TM5 chemical transport model in operational TROPOMI data retrieval results in systematic underestimations of surface pollution and overestimations of NO_2 at higher altitudes (Riess et al., 2022). These biases, while not insignificant, can contribute to discrepancy between estimates and inventories, with variations in surface albedo in different terrains potentially exacerbating the issue.

4.3.2 Limitations of divergence flux method

The Divergence Flux method has emerged as a powerful tool for quantifying global NO_x emissions using TROPOMI-derived NO_2 column density. However, like any methodology, it has limitations and uncertainties. In this section, we shed light on these aspects, underlining the critical points of consideration for researchers and policymakers.

In our quest for estimating NO_x emission from oil and gas operations, we navigate a landscape of uncertainties inherent to the divergence flux method. Previous studies have highlighted the relatively minor impact of wind-level altitude and the NO_x to NO_2 scaling factor on potential errors in emission estimates (Beirle et al., 2019, 2021). In contrast, more significant errors are associated with the background correction process, the selection of wind fields, and variations in OH lifetime, further emphasizing the complexity of accurate NO_x emission calculations (Dix et al., 2022). The uncertainty stemming from background correction serves as an essential indicator for assessing potential errors in emissions quantification. This uncertainty holds more weight in smaller study areas and regions with dynamically changing topography. To counteract its impact, adapting the background region becomes imperative. Furthermore, errors in

wind fields may lead to inaccuracies in divergence maps and hinder the spatial alignment of calculated emissions with actual sources. To address these challenges, a topography-wind" correction term was introduced (as outlined in Eq. 5) to effectively accounts for 3D transport effects. Employing the topography-wind term helps reduce uncertainties and enhance the accuracy of emission estimates. This approach aligns with a broader effort to improve the reliability of emissions data in complex terrains, providing a valuable tool for emissions quantification in challenging geographic regions. Furthermore, incorporating the topography-wind correction term with a scaling factor (f) of 1.5, representing an estimated net NO_x scale height of 667 meters, is a practical approach when regional-specific NO_x scale height information is lacking. As highlighted by Beirle et al., (2023), an assumed relative uncertainty of 33% (equivalent to f values ranging from 1.0 to 2.0 or NO_x scale heights between 500 and 1000 meters) is attributed to this topographic correction term. This uncertainty is subsequently propagated to the corrected advection map following Eq. 6.

Utilizing the divergence method for NO_x emission calculation relies on the premise of a steady state, implying consistent wind direction and uniform NO_x emissions within the region of interest. However, this daily divergence calculation assumption isn't universally valid. Regions characterized by systematic diurnal wind direction variations or intricate mesoscale meteorological dynamics beyond the spatial resolution of wind fields are ill-suited for the application of divergence method. Such areas pose challenges to the accuracy and suitability of method.

Tropospheric NO_2 columns are profoundly influenced by wind fields, significantly impacting the computation of NO_x emissions and lifetimes. To enhance data reliability, we implemented a filtering criterion, exclusively incorporating measurements associated with wind speeds exceeding 2 m s^{-1}. Given the limited lifetime of NO_2, satellite-based NO_2 distributions primarily reflect wind conditions during overpasses. Nevertheless, days with swiftly changing wind directions can distort spatial patterns, particularly manifesting as curved plumes. This distortion, more pronounced during extended lifetimes, significantly impacts single-day estimates. However, this influence diminishes when analyzing larger averages unaffected by frequent wind direction shifts. Despite the importance of wind conditions, it remains a substantial source of uncertainty, with reported variations of up to 20% in emissions when wind speeds are altered by 20%. Accurate global wind data is challenging to acquire, carrying an estimated 30% uncertainty. Uncertainties related to wind fields may vary across source regions, with an overall assumption of 30% uncertainty in our analyses (Beirle et al., 2011; Lorente et al., 2019).

For estimating NO_x emission, we implemented a novel approach involving the conversion of each TROPOMI pixel from NO_2 column density to NO_x column density. Our approach employed leverages the Leighton photostationary state principle to characterize the dynamic of polluted air masses (Karl et al., 2023; Leighton, 1961). This approach offers a great precision relative to conventional approaches that rely on constant conversion factors (~1.32). This improvement provides a significant advantage for our extensive analysis spanning a wide latitudinal gradients and seasonal variations. However, it is important to acknowledge that the parameterization of photolysis rates, coupled with the application of temperature-dependent rate

constants and ozone concentrations obtained from the ESCiMO dataset interpolated to the Sentinel 5P overpass time, introduces systematic uncertainties in the conversion process from NO_2 to NO_x.

In the assessment of NO_x emissions, it is imperative to consider the susceptibility of sink term to uncertainties in OH lifetimes. An erroneous estimation of the sink term could lead to erroneous negative emissions in various regions or, conversely, non-emitting areas with artificially elevated NO_x emissions. Although annual averaged emissions appear stable, daily and monthly maps reveal noteworthy patterns, with certain periods exhibiting negative emissions in some territories, while others display anomalous spikes in emissions, especially over deserts and seas during the summer. This suggests potential underestimations in the sink term during winter and spring and overestimations during summer, likely linked to OH estimation errors or additional sinks in the warmer months. Taking this into consideration, while the averaged emissions for the year 2022 remain unaffected, it serves to diminish the seasonal variations in emissions. A sensitivity analysis in the Delaware basin by (Dix et al., 2022) demonstrates a minor 13% deviation between parameterized OH values and WRF-Chem OH, despite the latter has higher variability. Consequently, the inclusion of this factor aids in alleviating errors in the calculated NO_x emissions, as it adjusts the proportion attributed to the sink term within the total emissions.

In summary, the comprehensive evaluation of NO_x emissions and lifetimes derived from TROPOMI NO_2 data grapples with a spectrum of error sources, primarily systematic in nature. These errors remain unaffected by extended temporal averaging, invariably leading to a consistent underestimation in estimated emissions. This underestimation predominantly stems from systematic discrepancies embedded in the TROPOMI NO_2 tropospheric column (30%–60%) and the wind field (30%). Furthermore, the variability in area size contributes an estimated 10% uncertainty, introducing a tendency for low-biased emissions and lifetimes. Other factors, encompassing uncertainty in the measurement time, clear-sky bias, and assumptions regarding sources, tend to accentuate this underestimation. Unraveling these intricacies necessitates in-depth investigations. Aggregating these error components, computed as squared values, yields an overall uncertainty estimate spanning the 40%–50% range.

5 Exploring the relationship: NOx emission, Oil & Gas production and methane enhancement

In recent environmental research, the intricate relationship between emissions and production volumes in the OG sector has garnered significant attention. Seminal studies by (Omara et al., 2022) and (de Gouw et al., 2020) have been instrumental in shaping this disclosure, primarily elucidating the interconnected dynamics between methane emissions and OG production. Omara et al., (2022) notably focused on methane emission at low-production OG sites, emphasizing the pivotal role of equipment maintenance in mitigating emissions. Conversely, (de Gouw et al., 2020)) conducted an extensive examination of the Permian Basin, revealing correlated columnar methane with OG production. Their findings highlighted the intricate correlation between emission, specifically methane and the volume of OG produced. Building upon the insights from these refence studies, our current research advances this exploration into a critical yet less-explored

dimension — the correlation between NO_x emissions and OG production volumes. NO_x is predominantly associated with combustion processes inherent in various facets of OG operations. Drawing inspiration from the previous studies, our study seeks to unravel the correlation between tropospheric NO_x emission and the intricate production dynamics of the OG industry, focusing on flaring activity.

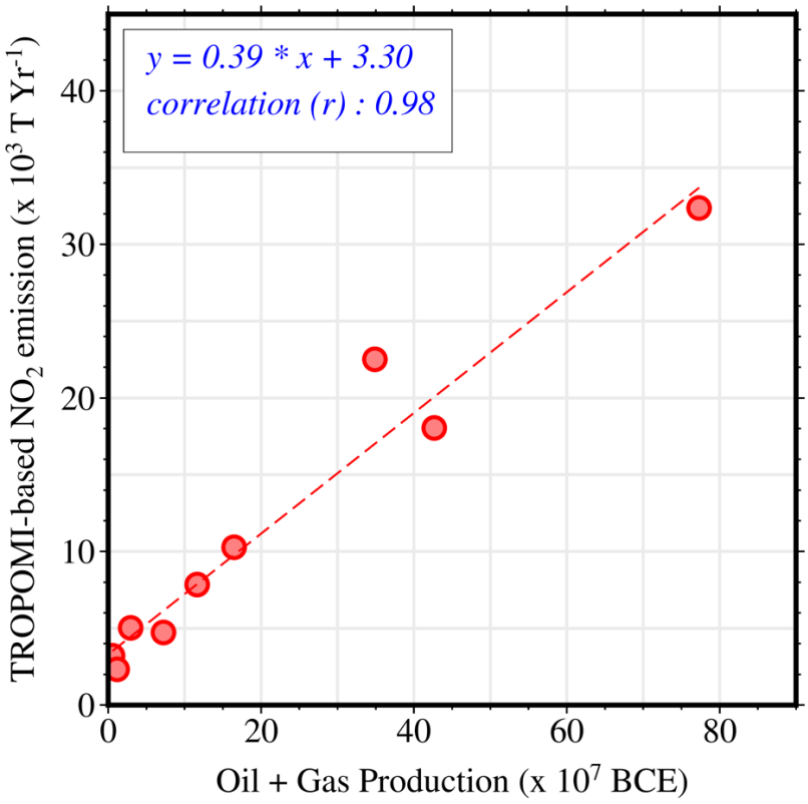

Figure 7: *Correlation between TROPOMI-derived NOx emissions and the oil and gas productions from the various OG sites.*

To facilitate this investigation, we acquired area-aggregated OG production data and well count information for the year 2022 from Enverus Prism (Enverus, 2023) and the Mexico Government's National Hydrocarbons Commission (CNH, 2023). This dataset, spanning nine discrete OG sites across the United States, Canada, and Mexico, offers a diversified representation of production activities within North America. The analytical emphasis revolves around comparing the annual mean production of oil and gas with the annual mean of NO_x emissions derived from TROPOMI observations. Our empirical findings revealed a robust correlation ($r = 0.98$ with $p <<< 0.001$) between TROPOMI-derived NO_x emissions and the integrated oil and gas productions for the selected OG sites (as seen in Figure 7). Notably, the site with the maximum OG productions exhibited the highest NO_x emission. This robust correlation, akin to prior observations on methane, underscores the intrinsic association between emissions and production volumes. These preliminary insights contribute substantively to the advancing discourse on emissions emanating

from OG operations. Our research delves beyond methane-centric investigations, uncovering the boarder environmental impact of OG activities. Understanding the crucial link between NO_x emissions and production volumes is pivotal for informed environmental management and policy decisions. This preliminary analysis sets the stage for more in-depth investigations, warranting consideration of additional factors and potentially expanding the scope of the study to other regions.

5.1 Exploring the relation: NO_2 with CH4 enhancement

The above exploration has also suggested that NO_x emissions from oil and gas operations may be accompanied by CH_4 emissions which is associated with OG production (Alvarez et al. 2018), which we explore in this study. NO_x and CH_4 emissions follow distinct routes: NO_x arises from combustion processes, while CH_4 results from fugitive or vented sources or gas flaring activity. While originating from distinct sources (Warneke et al., 2014), CH_4 and NO_x emissions in oil and gas operations exhibit a spatial correlation due to their close proximity during release (de Gouw et al., 2020; Gorchov Negron et al., 2018). This proximity creates a perception of emissions from a single source, impacting atmospheric measurements.

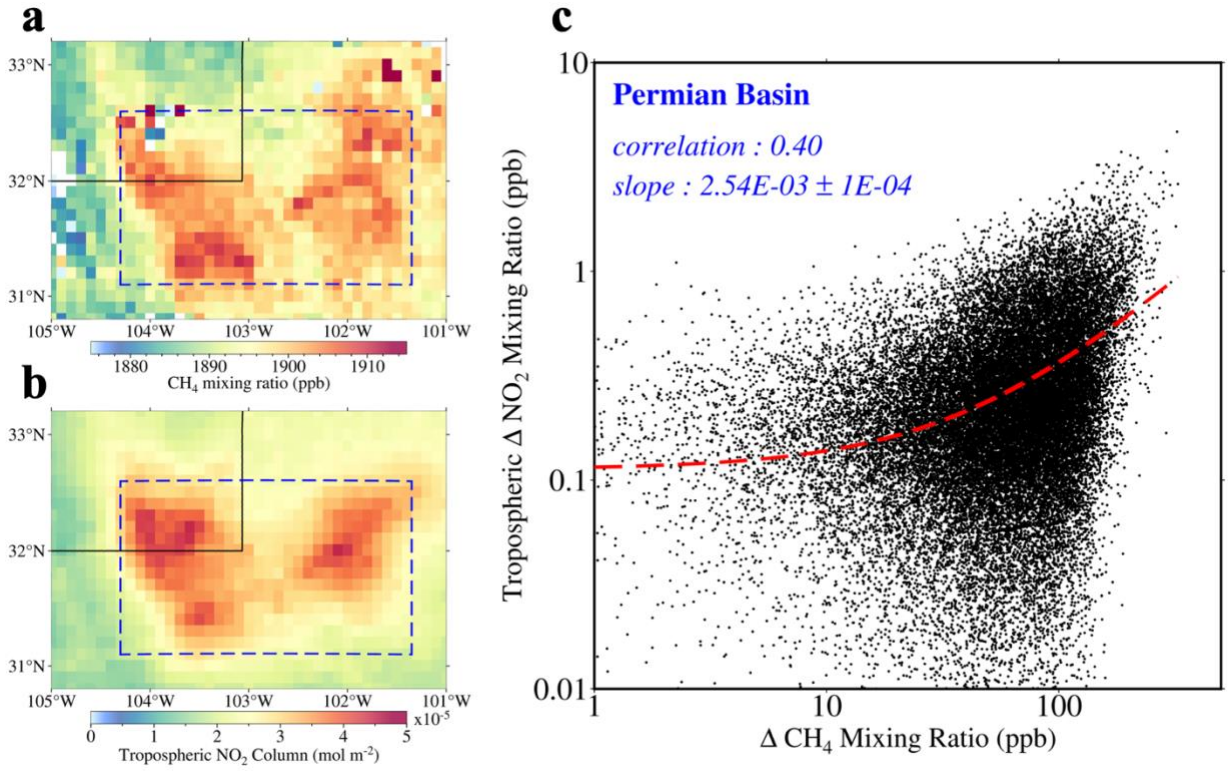

Figure 8: *Correlation between CH_4 and NO_2 columns in the Permian Basin using TROPOMI datasets. TROPOMI-derived (a) CH_4 mixing ratio and (b) tropospheric NO_2 column density over the Permian basin averaged from January - December 2022. (c) Correlation between enhancements of NO_x and CH_4 boundary layer mixing ratio across the Permian basin (highlighted by the thick red dashed line) observed from TROPOMI measurements during the period 2022. Linear fit (red dashed lines), the 95% confidence intervals of the slopes, and corresponding correlation values are shown.*

Figure 8a and 8b illustrate the averaged NO_2 column density and CH_4 mixing ratio over the Permian basin (area covered within blue box) encompassing the entire year of 2022. NO_2 and CH_4 exhibit elevated concentrations across the Delaware sub-basin in the western region and the Midland in the eastern sector of the Permian basin. The annual average for NO_2 and CH_4 displayed a correlation with a coefficient of 0.41, aligning closely with the correlation value reported by de Gouw et al., (2020) for the December 2018 to March 2019 period. We systematically explore the connection within the boundary layer between NO_2 and CH_4. We initiate our approach by deducing background values for both NO_2 and CH_4, aligning with the methodology presented by de Gouw et al. (2020). This process entails the calculation of the 10th percentile for each species. Following this initial step, we proceed to convert the NO_2 columns and CH_4 mixing ratios into boundary layer mixing ratios, by assuming a boundary layer thickness of 100 hPa. For CH_4, we adjust the column mixing ratio by dividing the surface pressure by 100 hPa, while for NO_2, this transformation involves a shift from number concentrations to mixing ratios. Subsequently, we employ orthogonal least-squares fitting to establish a linear correlation between the NO_2-CH_4 data points. Prior to conducting this fitting, we apply a scaling procedure to normalize both NO_2 and CH_4 values within the range of 0–1. Importantly, it's worth noting that this comprehensive analysis is tailored to days when over 10 sets of NO_2-CH_4 data are available, ensuring the robustness of our findings.

The analysis of the annual average $\Delta NO_x/\Delta CH_4$ ratio in the Permian Basin for the year 2022 yielded a value of $(2.54 \pm 0.1) \times 10^{-3}$. This result is lower than previously reported ratios, where Gorchov Negron et al., (2018) observed a considerably higher ratio of $(9.0 \pm 0.2) \times 10^{-3}$ through airborne measurements. Similarly, de Gouw et al., (2020) documented values of $(4.9 \pm 0.2) \times 10^{-3}$ for January 31, 2019, and approximately 3.0×10^{-3} for the December 2018 to March 2019 timeframe utilizing TROPOMI datasets. The variations in the observed $\Delta NO_x/\Delta CH_4$ ratios may be attributed to multiple factors. The variations in emission sources and their temporal dynamics across the different study periods could account for these differences. The 2022 timeframe may have witnessed alterations in emission patterns, or the development of the basins compared to the earlier periods under examination. In addition, the differences in the observed ratio can be explained by the composition of NO_x. NO_x encompasses both NO and NO_2, and the photochemical removal of NO_x can be significant during the atmospheric transport process across the basin. This removal process could lead to a reduction in the observed $\Delta NO_x/\Delta CH_4$ ratio in this study compared to the earlier studies. These findings contribute to a more comprehensive understanding of emission pattern from the OG fields.

Table 2: *Summary of observed $\Delta NO_x/\Delta CH_4$ ratios across the individual oil and gas basins over the period 2022.*

Basin	**$\Delta NO_x/\Delta CH_4$ ratio** ($\times 10^{-3}$)
Delaware (Permian basin), USA	3.0 ± 0.3
Midland (Permian basin), USA	2.5 ± 0.2

Eagle Ford, USA	6.2 ± 1.0
Bakken, USA	1.4 ± 1.0
Sureste onshore, Mexico	6.8 ± 2.0
Sureste offshore, Mexico	1.1 ± 0.5
Misantla onshore, Mexico	3.5 ± 1.0
Athabasca basin, Canada	5.2 ± 2.0
Grande Prairie, Canada	0.5 ± 1.3

In 2022, the TROPOMI-based observations unveiled distinctive $\Delta NO_x/\Delta CH_4$ ratios across various oil and gas basins in North America (Table 2), each offering a unique perspective on the regional emissions landscape. We examined the $\Delta NO_x/\Delta CH_4$ ratios separately for two regions within the larger Permian basin: Delaware and Midland. The Delaware basin displayed a relatively balanced ratio of $(3.0 \pm 0.3) \times 10^{-3}$. In contrast, the Midland basin, also part of the Permian basin, showed a slightly lower ratio of $(2.5 \pm 0.2) \times 10^{-3}$, emphasizing a greater prevalence of CH_4 emissions. On the other hand, the Eagle Ford basin in the U.S. reported a notably higher ratio of $(6.2 \pm 1.0) \times 10^{-3}$, indicating a prominent role of NO_x in emissions, warranting closer environmental scrutiny. Meanwhile, the Bakken basin displayed a low ratio of $(1.4 \pm 1.0) \times 10^{-3}$, signaling relatively modest emissions of both pollutants. In Mexico, the Sureste onshore region displayed a high $\Delta NO_x/\Delta CH_4$ ratio of $(6.8 \pm 2.0) \times 10^{-3}$, likely associated with industrial activities. Conversely, the Sureste offshore area had a low ratio of $(1.1 \pm 0.5) \times 10^{-3}$, while the Misantla onshore area showed a balanced ratio of $(3.5 \pm 1.0) \times 10^{-3}$. In Canada, the Athabasca basin indicated significant NO_x emissions with a ratio of $(5.2 \pm 2.0) \times 10^{-3}$, while Grande Prairie in Canada had the lowest ratio of $(0.5 \pm 1.3) \times 10^{-3}$, suggesting minimal emissions of both pollutants. These variations in $\Delta NO_x/\Delta CH_4$ ratios provide insights into the diverse emissions characteristics across these basins, contributing to our understanding of methane and NO_x emissions in the region.

6 Conclusion

In this comprehensive research study, we delve into the characteristics of NO_x emissions, focusing on 44 oil and gas production sites distributed across the globe. Leveraging the capabilities of satellite observations, we combine NO_2 data from TROPOMI with VIIRS-derived natural gas flaring detection, effectively pinpointing natural gas flaring hotspots. Drawing from established methodologies, we merge TROPOMI tropospheric NO_2 vertical column measurements with wind data sourced from ECMWF ERA5 reanalysis, applying the divergence flux method to uncover the nuanced dynamics of NO_x emissions. Benefitting from the high spatial resolution and high signal-to-noise ratio of TROPOMI measurements, our analysis encompasses the entire year of 2022, allowing us to analyze both the geographically diverse oil and gas emission sources that have rarely been explored previously and the temporal variability over short-term intervals. This study

encompasses a total of 44 oil and gas production fields located in diverse regions across the globe, providing a comprehensive examination of NO_x emissions in this critical industry.

Our extensive global assessment compared NO_x emissions derived from TROPOMI with two established inventories, EDGARv6.1 (2018) and CAMS-GLOB-ANT_v5.3 (2019-2022). Notably, our findings revealed significant discrepancies between TROPOMI-based estimates and the inventories. TROPOMI reported higher emission levels, likely indicating the need for improved accuracy in emission inventories, particularly within the oil and gas sectors. We then delved into site-specific comparisons, analyzing 44 oil and gas production regions worldwide. The outcomes emphasized the benefits of high-resolution measurements from TROPOMI in assessing emissions, especially in regions with discrepancies between inventories. The differences were attributed to various factors, including the influence of urban areas, dynamic nature of emissions, and wind patterns. Furthermore, in our analysis comparing onshore and offshore oil and gas production sites, distinct quantitative findings emerged, shedding light into the performance of emission inventories (EDGAR and CAMS) in these different settings. For onshore sites, where the influence of urban areas and associated emissions is more pronounced, both EDGAR and CAMS exhibited substantial underestimations in comparison to TROPOMI-derived NO_x emissions. Specifically, EDGAR underestimated emissions by an average of approximately 61%, while CAMS showed a more significant underestimation, averaging around 78%. Conversely, for offshore sites, characterized by their remote location and reduced impact from urban emissions, EDGAR's performance notably improved. It exhibited a much lower average underestimation of approximately 26% compared to TROPOMI-derived NO_x emissions. In contrast, CAMS continued to struggle with offshore sites, displaying a substantial underestimation of approximately 92% on average. These quantitative differences underscore the intricate interplay between emissions from various sources and background contributions, highlighting the necessity of implementing region-specific environmental management strategies. These findings may provide valuable insights for policymakers and environmental scientists seeking to enhance emission inventories related to oil and gas operations, emphasizing the importance of tailored approaches for onshore and offshore settings. Moreover, the divergence method applied in this study to satellite data offers an effective solution to address the inherent challenges associated with general bottom-up emission inventories in the context of oil and gas operations. Its benefits include the provision of near-real time emissions data for applications such as chemistry transport models, the critical role of evaluating existing emission inventories, and the ability to furnish granular insights into the spatial distribution of NO_x emissions, thus reducing uncertainties.

Our study has rigorously examined uncertainties in estimating NO_2 and NO_x emissions from global oil and gas fields using TROPOMI datasets and the flux divergence method. These uncertainties, originating from both data sources and the method itself, are essential to acknowledge for reliable emissions data. The quantification of these uncertainties is paramount for ensuring the accuracy and reliability of emissions data, which, in turn, informs critical policy and decision-making processes. Precisely estimating tropospheric NO_2 column density confronts challenges, including measurement noise, spectral fitting errors, and distinguishing between

stratospheric and tropospheric NO_2. Calculating tropospheric air mass factors amplifies uncertainties, influenced by surface albedo, cloud fraction, and aerosol assumptions, ranging from 30% to 60%. This underscores the ongoing need for data quality and retrieval algorithm enhancements. Satellite data use introduces biases, such as clear-sky bias, temporal bias, and those tied to air mass factor estimation and local effects. Recent TROPOMI versions exhibit variable tropospheric vertical column densities, adding complexity. We explore limitations in the divergence flux method, encompassing uncertainties in background correction, wind field selection, OH lifetime variations, and daily divergence calculations. Wind fields present substantial uncertainties affecting NO_x emission accuracy and divergence map reliability. Furthermore, our novel approach converts NO_2 to NO_x column density, stressing precision. However, this process introduces systematic errors related to photolysis frequencies, rate constants, and ozone concentrations. OH lifetime uncertainties affect the sink term, potentially leading to erroneous emissions. In summary, the assessment of NO_x emissions and lifetimes from TROPOMI NO_2 data consistently reveals systematic errors, resulting in underestimations of emissions by 40% to 50%. Recognizing and quantifying these uncertainties are pivotal for enhancing data accuracy and informed decision-making in environmental policies.

Furthermore, we explored the correlation between tropospheric NOx emissions and oil and gas (OG) production volumes. Analyzing data from nine diverse North American OG sites, a robust correlation ($r = 0.98$) between TROPOMI-derived NOx emissions and integrated oil and gas production highlights the intrinsic link between emissions and production volumes, offering crucial insights for environmental management and policy decisions in the OG sector. In addition, our study underscores the co-emission of NO_x and CH_4 from oil and gas operations, despite their distinct sources. Through an analysis of $\Delta NO_x/\Delta CH_4$ ratios, we have identified variations in emissions characteristics, shedding light on the intricate interplay between pollutants and their sources. Our findings contribute to a more comprehensive understanding of methane and NO_x emissions in diverse geographic regions, providing insights of continuous monitoring and region-specific strategies for air pollution management and mitigation efforts.

Acknowledgment

We thank ESA and the TROPOMI L1/L2 teams for realizing TROPOMI and providing NO_2 tropospheric data. ERA-Interim and ERA-5 data used in this study are provided by the European Centre for Medium-Range Weather Forecasts (ECMWF). The EMAC simulations have been performed at the German Climate Computing Centre (DKRZ) through support from the Bundesministerium für Bildung und Forschung (BMBF). DKRZ and its scientific steering committee are gratefully acknowledged for providing the HPC and data archiving resources for this consortial project ESCiMo (Earth System Chemistry integrated Modelling). Jöckel Patrick is acknowledged for providing the ESCiMo model data used for the ozone climatology. We greatly appreciate inputs from Daniel Zavala-Araiza, Kang Sun and Yuzhong Zhang and for their useful discussions during the preparation of this work.

Data Availability

The TROPOMI NO_2 product is publicly available on the TROPOMI Open hub (http://www.tropomi.eu/data-products/data-access, TROPOMI DataHub, 2022). The European Centre for Medium-Range Weather Forecasts (ECMWF) ERA5 reanalysis be downloaded from the Copernicus Climate Data Store (https://cds.climate.copernicus.eu/cdsapp#!/dataset/reanalysis-era5-pressure-levels-monthly-means, ECMWF, 2022b). EDGARv6.1 emissions are provided by https://edgar.jrc.ec.europa.eu/emissions_data_and_maps. CAMS-GLOB-ANT_v5.3 emissions are available at https://eccad3.sedoo.fr. CAMS data can be downloaded from the Copernicus Climate Data Store (https://ads.atmosphere.copernicus.eu/cdsapp#!/dataset/cams-global-atmospheric-composition-forecasts, ECMWF, 2022a).

Author contributions. PNP and RG designed the study. PNP performed the analysis and interpretation of the various satellite and emission datasets used in the study. RG supervised the study and contributed to the data analysis and interpretation. MO contributed to the data analysis of flaring and production data. PNP wrote the draft with inputs from all coauthors.

Competing interests. The authors declare that they have no conflict of interest.

References

Alvarez, R. (2018). Assessment of methane emissions from the U.S. oil and gas supply chain. *Science*, *361*, 186–188.

Atkinson, R. , Baulch, D. L. , Cox, R. A. , Crowley, J. N. , Hampson, R. F. , Hynes, R. G. , Jenkin, M. E. , Rossi, M. J. , & Troe, J. (2004). *IUPAC Task Group on Atmospheric Chemical Kinetic Data Evaluation, data sheet last evaluated: June 2013*. http://iupac.pole-ether.fr

Banerjee, S. D., & Toledano, P. (2016). *A Policy Framework to Approach the Use of Associated Petroleum Gas*. https://doi.org/10.7916/D8028RQ8

Beirle, S., Boersma, K. F., Platt, U., Lawrence, M. G., & Wagner, T. (2011). Megacity emissions and lifetimes of nitrogen oxides probed from space. *Science*, *333*(6050), 1737–1739. https://doi.org/10.1126/SCIENCE.1207824

Beirle, S., Borger, C., Dörner, S., Eskes, H., Kumar, V., De Laat, A., & Wagner, T. (2021). Catalog of NOx emissions from point sources as derived from the divergence of the NO2 flux for TROPOMI. *Earth System Science Data*, *13*(6), 2995–3012. https://doi.org/10.5194/ESSD-13-2995-2021

Beirle, S., Borger, C., Dörner, S., Li, A., Hu, Z., Liu, F., Wang, Y., & Wagner, T. (2019). Pinpointing nitrogen oxide emissions from space. *Science Advances*, *5*(11). https://doi.org/10.1126/SCIADV.AAX9800

Beirle, S., Borger, C., Jost, A., & Wagner, T. (2023). Improved catalog of NOx point source emissions (version 2). *Earth System Science Data*, *15*(7), 3051–3073. https://doi.org/10.5194/ESSD-15-3051-2023

Boersma, K. F., Eskes, H. J., & Brinksma, E. J. (2004). Error analysis for tropospheric NO2 retrieval from space. *Journal of Geophysical Research: Atmospheres*, *109*(4). https://doi.org/10.1029/2003JD003962

Boersma, K. F., Eskes, H. J., Veefkind, J. P., Brinksma, E. J., Van Der A, R. J., Sneep, M., Van Den Oord, G. H. J., Levelt, P. F., Stammes, P., Gleason, J. F., & Bucsela, E. J. (2007). Near-real time retrieval of tropospheric NO2 from OMI. *Atmospheric Chemistry and Physics*, *7*(8), 2103–2118. https://doi.org/10.5194/ACP-7-2103-2007

de Gouw, J. A., Veefkind, J. P., Roosenbrand, E., Dix, B., Lin, J. C., Landgraf, J., & Levelt, P. F. (2020). Daily Satellite Observations of Methane from Oil and Gas Production Regions in the United States. *Scientific Reports 2020 10:1*, *10*(1), 1–10. https://doi.org/10.1038/s41598-020-57678-4

De Smedt, I., Theys, N., Yu, H., Danckaert, T., Lerot, C., Compernolle, S., Van Roozendael, M., Richter, A., Hilboll, A., Peters, E., Pedergnana, M., Loyola, D., Beirle, S., Wagner, T., Eskes, H., Van Geffen, J., Folkert Boersma, K., & Veefkind, P. (2018). Algorithm theoretical baseline for formaldehyde retrievals from S5P TROPOMI and from the QA4ECV project. *Atmospheric Measurement Techniques*, *11*(4), 2395–2426. https://doi.org/10.5194/AMT-11-2395-2018

Dickerson, R. R., Stedman, D. H., & Delany, A. C. (1982). Direct measurements of ozone and nitrogen dioxide photolysis rates in the troposphere. *Journal of Geophysical Research*, *87*(C7), 4933–4946. https://doi.org/10.1029/JC087IC07P04933

Dix, B., de Bruin, J., Roosenbrand, E., Vlemmix, T., Francoeur, C., Gorchov-Negron, A., McDonald, B., Zhizhin, M., Elvidge, C., Veefkind, P., Levelt, P., & de Gouw, J. (2020). Nitrogen Oxide Emissions from U.S. Oil and Gas Production: Recent Trends and Source Attribution. *Geophysical Research Letters*, *47*(1). https://doi.org/10.1029/2019GL085866

Dix, B., Francoeur, C., Li, M., Serrano-Calvo, R., Levelt, P. F., Veefkind, J. P., McDonald, B. C., & de Gouw, J. (2022). Quantifying NOx Emissions from U.S. Oil and Gas Production Regions Using TROPOMI NO2. *ACS Earth and Space Chemistry*, *6*(2), 403–414. https://doi.org/10.1021/ACSEARTHSPACECHEM.1C00387

Duncan, B. N., Lamsal, L. N., Thompson, A. M., Yoshida, Y., Lu, Z., Streets, D. G., Hurwitz, M. M., & Pickering, K. E. (2016). A space-based, high-resolution view of notable changes in urban NOx pollution around the world (2005–2014). *Journal of Geophysical Research*, *121*(2), 976–996. https://doi.org/10.1002/2015JD024121

Edwards, P. M., Brown, S. S., Roberts, J. M., Ahmadov, R., Banta, R. M., DeGouw, J. A., Dubé, W. P., Field, R. A., Flynn, J. H., Gilman, J. B., Graus, M., Helmig, D., Koss, A., Langford, A. O., Lefer, B. L., Lerner, B. M., Li, R., Li, S. M., McKeen, S. A., … Zamora, R. (2014). High winter ozone pollution from carbonyl photolysis in an oil and gas basin. *Nature*, *514*(7522), 351–354. https://doi.org/10.1038/NATURE13767

Elvidge, C. D., Bazilian, M. D., Zhizhin, M., Ghosh, T., Baugh, K., & Hsu, F. C. (2018). The potential role of natural gas flaring in meeting greenhouse gas mitigation targets. *Energy Strategy Reviews*, *20*, 156–162. https://doi.org/10.1016/J.ESR.2017.12.012

Elvidge, C. D., Zhizhin, M., Baugh, K., Hsu, F. C., & Ghosh, T. (2015). Methods for Global Survey of Natural Gas Flaring from Visible Infrared Imaging Radiometer Suite Data. *Energies 2016, Vol. 9, Page 14*, *9*(1), 14. https://doi.org/10.3390/EN9010014

Elvidge, C. D., Zhizhin, M., Hsu, F. C., & Baugh, K. E. (2013). VIIRS nightfire: Satellite pyrometry at night. *Remote Sensing*, *5*(9), 4423–4449. https://doi.org/10.3390/RS5094423

Falkner, R. (2016). The Paris agreement and the new logic of international climate politics. *International Affairs*, *92*(5), 1107–1125. https://doi.org/10.1111/1468-2346.12708

Fedkin, N. M., Stauffer, R. M., Thompson, A. M., Kollonige, D. E., Wecht, H. D., & Elguindi, N. (2024). Satellite NO2 Trends and Hotspots Over Offshore Oil and Gas Operations in the Gulf of Mexico. *Earth and Space Science*, *11*(3). https://doi.org/10.1029/2023EA003165

Fioletov, V. E., McLinden, C. A., Krotkov, N., Yang, K., Loyola, D. G., Valks, P., Theys, N., Van Roozendael, M., Nowlan, C. R., Chance, K., Liu, X., Lee, C., & Martin, R. V. (2013). Application of OMI, SCIAMACHY, and GOME-2 satellite SO2 retrievals for detection of large emission sources. *Journal of Geophysical Research Atmospheres*, *118*(19), 11399–11418. https://doi.org/10.1002/JGRD.50826

Francoeur, C. B., McDonald, B. C., Gilman, J. B., Zarzana, K. J., Dix, B., Brown, S. S., de Gouw, J. A., Frost, G. J., Li, M., McKeen, S. A., Peischl, J., Pollack, I. B., Ryerson, T. B., Thompson, C., Warneke, C., & Trainer, M. (2021). Quantifying Methane and Ozone Precursor Emissions from Oil and Gas Production Regions across the Contiguous US. *Environmental Science and Technology*, *55*(13), 9129–9139. https://doi.org/10.1021/ACS.EST.0C07352/ASSET/IMAGES/LARGE/ES0C07352_0006.JPEG

Gilman, J. B., Lerner, B. M., Kuster, W. C., & De Gouw, J. A. (2013). Source signature of volatile organic compounds from oil and natural gas operations in northeastern Colorado. *Environmental Science and Technology*, *47*(3), 1297–1305. https://doi.org/10.1021/ES304119A

Goldberg, D. L., Lu, Z., Streets, D. G., De Foy, B., Griffin, D., Mclinden, C. A., Lamsal, L. N., Krotkov, N. A., & Eskes, H. (2019). Enhanced Capabilities of TROPOMI NO2: Estimating NOX from North American Cities and Power Plants. *Environmental Science and Technology*, *53*(21), 12594–12601. https://doi.org/10.1021/ACS.EST.9B04488

Gorchov Negron, A. M., McDonald, B. C., McKeen, S. A., Peischl, J., Ahmadov, R., De Gouw, J. A., Frost, G. J., Hastings, M. G., Pollack, I. B., Ryerson, T. B., Thompson, C., Warneke, C., & Trainer, M. (2018). Development of a fuel-based oil and gas inventory of nitrogen oxides emissions. *Environmental Science & Technology*, *52*(17), 10175–10185. https://doi.org/10.1021/acs.est.8b02245

Granier, C., Darras, S., Denier van der Gon, H., Doubalova, J., Elguindi, N., Galle, B., Gauss, M., Guevara, M., Jalkanen, J.-P., Kuenen, J., Liousse, C., Quack, B., Simpson, D., & Sindelarova, K. (2019). *The Copernicus Atmosphere Monitoring Service global and regional emissions (April 2019 version)*.

Hersbach, H., Bell, B., Berrisford, P., Hirahara, S., Horányi, A., Muñoz-Sabater, J., Nicolas, J., Peubey, C., Radu, R., Schepers, D., Simmons, A., Soci, C., Abdalla, S., Abellan, X., Balsamo, G., Bechtold, P., Biavati, G., Bidlot, J., Bonavita, M., … Thépaut, J. N. (2020). The ERA5 global reanalysis. *Quarterly Journal of the Royal Meteorological Society*, *146*(730), 1999–2049. https://doi.org/10.1002/QJ.3803

Hoesly, R. M., Smith, S. J., Feng, L., Klimont, Z., Janssens-Maenhout, G., Pitkanen, T., Seibert, J. J., Vu, L., Andres, R. J., Bolt, R. M., Bond, T. C., Dawidowski, L., Kholod, N., Kurokawa, J. I., Li, M., Liu, L., Lu, Z., Moura, M. C. P., O'Rourke, P. R., & Zhang, Q. (2018). Historical (1750-2014) anthropogenic emissions of reactive gases and aerosols from the Community Emissions Data System (CEDS). *Geoscientific Model Development*, *11*(1), 369–408. https://doi.org/10.5194/GMD-11-369-2018

Ialongo, I., Stepanova, N., Hakkarainen, J., Virta, H., & Gritsenko, D. (2021). Satellite-based estimates of nitrogen oxide and methane emissions from gas flaring and oil production activities in Sakha Republic, Russia. *Atmospheric Environment: X*, *11*. https://doi.org/10.1016/J.AEAOA.2021.100114

Jacob, D. J. (1999). *Introduction to atmospheric chemistry*. Princeton University Press.

Janssens-Maenhout, G., Crippa, M., Guizzardi, D., Muntean, M., Schaaf, E., Dentener, F., Bergamaschi, P., Pagliari, V., Olivier, J. G. J., Peters, J. A. H. W., Van Aardenne, J. A., Monni, S., Doering, U., Roxana Petrescu, A. M., Solazzo, E., & Oreggioni, G. D. (2019). EDGAR v4.3.2 Global Atlas of the three major greenhouse gas emissions for the period 1970-2012. *Earth System Science Data*, *11*(3), 959–1002. https://doi.org/10.5194/ESSD-11-959-2019

Jenkin, M. E., Saunders, S. M., Wagner, V., & Pilling, M. J. (2003). Protocol for the development of the Master Chemical Mechanism, MCM v3 (Part B): Tropospheric degradation of aromatic volatile organic compounds. *Atmospheric Chemistry and Physics*, *3*(1), 181–193. https://doi.org/10.5194/ACP-3-181-2003

Jöckel, P., Kerkweg, A., Pozzer, A., Sander, R., Tost, H., Riede, H., Baumgaertner, A., Gromov, S., & Kern, B. (2010). Development cycle 2 of the Modular Earth Submodel System (MESSy2). *Geoscientific Model Development*, *3*(2), 717–752. https://doi.org/10.5194/GMD-3-717-2010

Jöckel, P., Tost, H., Pozzer, A., Kunze, M., Kirner, O., Brenninkmeijer, C. A. M., Brinkop, S., Cai, D. S., Dyroff, C., Eckstein, J., Frank, F., Garny, H., Gottschaldt, K. D., Graf, P., Grewe, V., Kerkweg, A., Kern, B., Matthes, S., Mertens, M., … Zahn, A. (2016). Earth System Chemistry integrated Modelling (ESCiMo) with the Modular Earth Submodel System (MESSy) version 2.51. *Geoscientific Model Development*, *9*(3), 1153–1200. https://doi.org/10.5194/GMD-9-1153-2016

Karl, T., Lamprecht, C., Graus, M., Cede, A., Tiefengraber, M., Vila-Guerau De Arellano, J., Gurarie, D., & Lenschow, D. (2023). *High urban NO x triggers a substantial chemical downward flux of ozone*. https://www.science.org

Keohane, R. O., & Oppenheimer, M. (2016). Paris: Beyond the climate dead end through pledge and review? *Politics and Governance*, *4*(3), 142–151. https://doi.org/10.17645/PAG.V4I3.634

Kleipool, Q. L., Dobber, M. R., de Haan, J. F., & Levelt, P. F. (2008). Earth surface reflectance climatology from 3 years of OMI data. *Journal of Geophysical Research Atmospheres*, *113*(18). https://doi.org/10.1029/2008JD010290

Laughner, J. L., & Cohen, R. C. (2019). Direct observation of changing NOx lifetime in North American cities. *Science*, *366*(6466), 723–727. https://doi.org/10.1126/SCIENCE.AAX6832

Lauvaux, T., Giron, C., Mazzolini, M., D'Aspremont, A., Duren, R., Cusworth, D., Shindell, D., & Ciais, P. (2022). Global assessment of oil and gas methane ultra-emitters. *Science*, *375*(6580). https://doi.org/10.1126/SCIENCE.ABJ4351

Leighton, P. (1961). *Photochemistry of Air Pollution 1st Edition*. *January 1*, 1–300. https://www.elsevier.com/books/photochemistry-of-air-pollution/leighton/978-0-12-442250-6

Li, C., Hsu, N. C., Sayer, A. M., Krotkov, N. A., Fu, J. S., Lamsal, L. N., Lee, J., & Tsay, S. C. (2016). Satellite observation of pollutant emissions from gas flaring activities near the Arctic. *Atmospheric Environment*, *133*, 1–11. https://doi.org/10.1016/J.ATMOSENV.2016.03.019

Liu, F., Beirle, S., Zhang, Q., Dörner, S., He, K., & Wagner, T. (2016). NOx lifetimes and emissions of cities and power plants in polluted background estimated by satellite observations. *Atmospheric Chemistry and Physics*, *16*(8), 5283–5298. https://doi.org/10.5194/ACP-16-5283-2016

Liu, S., Valks, P., Pinardi, G., Xu, J., Chan, K. L., Argyrouli, A., Lutz, R., Beirle, S., Khorsandi, E., Baier, F., Huijnen, V., Bais, A., Donner, S., Dörner, S., Gratsea, M., Hendrick, F., Karagkiozidis, D., Lange, K., Piters, A. J. M., … Loyola, D. G. (2021). An improved TROPOMI tropospheric NO2 research product over Europe. *Atmospheric Measurement Techniques*, *14*(11), 7297–7327. https://doi.org/10.5194/AMT-14-7297-2021

Lorente, A., Boersma, K. F., Eskes, H. J., Veefkind, J. P., van Geffen, J. H. G. M., de Zeeuw, M. B., Denier van der Gon, H. A. C., Beirle, S., & Krol, M. C. (2019). Quantification of nitrogen oxides emissions from build-up of pollution over Paris with TROPOMI. *Sci. Rep.*, *9*(1), 20033. https://doi.org/10.1038/s41598-019-56428-5

Lyon, D. R., Hmiel, B., Gautam, R., Omara, M., Roberts, K. A., Barkley, Z. R., Davis, K. J., Miles, N. L., Monteiro, V. C., Richardson, S. J., Conley, S., Smith, M. L., Jacob, D. J., Shen, L., Varon, D. J., Deng, A., Rudelis, X., Sharma, N., Story, K. T., … Hamburg, S. P. (2021). Concurrent variation in oil and gas methane emissions and oil price during the COVID-19 pandemic. *Atmospheric Chemistry and Physics*, *21*(9), 6605–6626. https://doi.org/10.5194/ACP-21-6605-2021

Majid, A., Martin, M. V., Lamsal, L. N., & Duncan, B. N. (2017). A decade of changes in nitrogen oxides over regions of oil and natural gas activity in the United States. *Elementa*, *5*. https://doi.org/10.1525/ELEMENTA.259

McLinden, C. A., Fioletov, V., Boersma, K. F., Krotkov, N., Sioris, C. E., Veefkind, J. P., & Yang, K. (2012). Air quality over the Canadian oil sands: A first assessment using satellite observations. *Geophysical Research Letters*, *39*(4). https://doi.org/10.1029/2011GL050273

McLinden, C. A., Fioletov, V., Shephard, M. W., Krotkov, N., Li, C., Martin, R. V., Moran, M. D., & Joiner, J. (2016). Space-based detection of missing sulfur dioxide sources of global air pollution. *Nature Geoscience*, *9*(7), 496–500. https://doi.org/10.1038/NGEO2724

Omara, M., Gautam, R., O'Brien, M. A., Himmelberger, A., Franco, A., Meisenhelder, K., Hauser, G., Lyon, D. R., Chulakadabba, A., Miller, C. C., Franklin, J., Wofsy, S. C., & Hamburg, S. P. (2023). Developing a spatially explicit global oil and gas infrastructure database for characterizing methane emission sources at high resolution. *Earth System Science Data*, *15*(8), 3761–3790. https://doi.org/10.5194/ESSD-15-3761-2023

Omara, M., Zavala-Araiza, D., Lyon, D. R., Hmiel, B., Roberts, K. A., & Hamburg, S. P. (2022). Methane emissions from US low production oil and natural gas well sites. *Nature Communications*, *13*(1). https://doi.org/10.1038/S41467-022-29709-3

Riess, T. C. V. W., Boersma, K. F., Van Vliet, J., Peters, W., Sneep, M., Eskes, H., & Van Geffen, J. (2022). Improved monitoring of shipping NO2 with TROPOMI: Decreasing NOx emissions in European seas during the COVID-19 pandemic. *Atmospheric Measurement Techniques*, *15*(5), 1415–1438. https://doi.org/10.5194/AMT-15-1415-2022

Rohrer, F., & Berresheim, H. (2006). Strong correlation between levels of tropospheric hydroxyl radicals and solar ultraviolet radiation. *Nature 2006 442:7099*, *442*(7099), 184–187. https://doi.org/10.1038/nature04924

Saunders, S. M., Jenkin, M. E., Derwent, R. G., & Pilling, M. J. (2003). Protocol for the development of the Master Chemical Mechanism, MCM v3 (Part A): Tropospheric

degradation of non-aromatic volatile organic compounds. *Atmospheric Chemistry and Physics*, *3*(1), 161–180. https://doi.org/10.5194/ACP-3-161-2003

Seinfeld, J. H., & Pandis, S. N. (2016). Atmospheric Chemistry and Physics: From Air Pollution to Climate Change. In *John Wiley & Sons, Inc., Hoboken, New Jersey* (3rd ed.). John Wiley & Sons, Inc., Hoboken, New Jersey.

Shaiganfar, R., Beirle, S., Sharma, M., Chauhan, A., Singh, R. P., & Wagner, T. (2011). Estimation of NO x emissions from Delhi using Car MAX-DOAS observations and comparison with OMI satellite data. *Atmos. Chem. Phys.*, *11*(21), 10871–10887. https://doi.org/10.5194/acp-11-10871-2011

Shen, L., Gautam, R., Omara, M., Zavala-Araiza, D., Maasakkers, J. D., Scarpelli, T. R., Lorente, A., Lyon, D., Sheng, J., Varon, D. J., Nesser, H., Qu, Z., Lu, X., Sulprizio, M. P., Hamburg, S. P., & Jacob, D. J. (2022). Satellite quantification of oil and natural gas methane emissions in the US and Canada including contributions from individual basins. *Atmospheric Chemistry and Physics*, *22*(17), 11203–11215. https://doi.org/10.5194/ACP-22-11203-2022

Simpson, I. J., Blake, N. J., Barletta, B., Diskin, G. S., Fuelberg, H. E., Gorham, K., Huey, L. G., Meinardi, S., Rowland, F. S., Vay, S. A., Weinheimer, A. J., Yang, M., & Blake, D. R. (2010). Characterization of trace gases measured over alberta oil sands mining operations: 76 speciated C2-C10 volatile organic compounds (VOCs), CO2, CH4, CO, NO, NO2, NOy, O3 and SO2. *Atmospheric Chemistry and Physics*, *10*(23), 11931–11954. https://doi.org/10.5194/ACP-10-11931-2010

Van Geffen, J., Eskes, H., Compernolle, S., Pinardi, G., Verhoelst, T., Lambert, J. C., Sneep, M., Linden, M. Ter, Ludewig, A., Folkert Boersma, K., & Pepijn Veefkind, J. (2021). Sentinel-5P TROPOMI NO2retrieval: impact of version v2.2 improvements and comparisons with OMI and ground-based data. *Atmospheric Measurement Techniques*, *15*(7), 2037–2060. https://doi.org/10.5194/AMT-15-2037-2022

Van Geffen, J., Eskes, H., Compernolle, S., Pinardi, G., Verhoelst, T., Lambert, J. C., Sneep, M., Linden, M. Ter, Ludewig, A., Folkert Boersma, K., & Pepijn Veefkind, J. (2022). Sentinel-5P TROPOMI NO2retrieval: impact of version v2.2 improvements and comparisons with OMI and ground-based data. *Atmospheric Measurement Techniques*, *15*(7), 2037–2060. https://doi.org/10.5194/AMT-15-2037-2022

Van Geffen, J., Folkert Boersma, K., Eskes, H., Sneep, M., Ter Linden, M., Zara, M., & Pepijn Veefkind, J. (2020). S5P TROPOMI NO2 slant column retrieval: Method, stability, uncertainties and comparisons with OMI. *Atmospheric Measurement Techniques*, *13*(3), 1315–1335. https://doi.org/10.5194/AMT-13-1315-2020

Varon, D. J., Jervis, D., Pandey, S., Gallardo, S. L., Balasus, N., Yang, L. H., & Jacob, D. J. (2024). Quantifying NOx point sources with Landsat and Sentinel-2 satellite observations of NO2 plumes. *Proceedings of the National Academy of Sciences of the United States of America*, *121*(27), e2317077121. https://doi.org/10.1073/PNAS.2317077121/SUPPL_FILE/PNAS.2317077121.SAPP.PDF

Warneke, C., Geiger, F., Edwards, P. M., Dube, W., Pétron, G., Kofler, J., Zahn, A., Brown, S. S., Graus, M., Gilman, J. B., Lerner, B. M., Peischl, J., Ryerson, T. B., De Gouw, J. A., & Roberts, J. M. (2014). Volatile organic compound emissions from the oil and natural gas industry in the Uintah Basin, Utah: oil and gas well pad emissions compared to ambient air composition. *Atmospheric Chemistry and Physics*, *14*(20), 10977–10988. https://doi.org/10.5194/acp-14-10977-2014

WHO. (2019). Ambient (outdoor) air quality and health. In *Who*. http://www.who.int/airpollution/en/ (accessed on 30 March 2019)

Williams, J. E., Folkert Boersma, K., Le Sager, P., & Verstraeten, W. W. (2017). The high-resolution version of TM5-MP for optimized satellite retrievals: Description and validation. *Geoscientific Model Development*, *10*(2), 721–750. https://doi.org/10.5194/GMD-10-721-2017

Zavala-Araiza, D., Lyon, D., Alvarez, R. A., Palacios, V., Harriss, R., Lan, X., Talbot, R., & Hamburg, S. P. (2015). Toward a Functional Definition of Methane Super-Emitters: Application to Natural Gas Production Sites. *Environmental Science and Technology*, *49*(13), 8167–8174. https://doi.org/10.1021/ACS.EST.5B00133

Zhang, Y., Gautam, R., Pandey, S., Omara, M., Maasakkers, J. D., Sadavarte, P., Lyon, D., Nesser, H., Sulprizio, M. P., Varon, D. J., Zhang, R., Houweling, S., Zavala-Araiza, D., Alvarez, R. A., Lorente, A., Hamburg, S. P., Aben, I., & Jacob, D. J. (2020). Quantifying methane emissions from the largest oil-producing basin in the United States from space. *Science Advances*, *6*(17). https://doi.org/10.1126/SCIADV.AAZ5120

Zhang, Y., Gautam, R., Zavala-Araiza, D., Jacob, D. J., Zhang, R., Zhu, L., Sheng, J. X., & Scarpelli, T. (2019). Satellite-Observed Changes in Mexico's Offshore Gas Flaring Activity Linked to Oil/Gas Regulations. *Geophysical Research Letters*, *46*(3), 1879–1888. https://doi.org/10.1029/2018GL081145

Zhu, L., Jacob, D. J., Mickley, L. J., Marais, E. A., Cohan, D. S., Yoshida, Y., Duncan, B. N., Abad, G. G., & Chance, K. V. (2014). Anthropogenic emissions of highly reactive volatile organic compounds in eastern Texas inferred from oversampling of satellite (OMI) measurements of HCHO columns. *Environmental Research Letters*, *9*(11). https://doi.org/10.1088/1748-9326/9/11/114004